Depth Dependent Focal Mechanisms of Volcanic Deep Low-Frequency Earthquakes in Northeast Japan

Genki Oikawa[1], Naofumi Aso[1], and Junichi Nakajima[1]

[1]Tokyo Institute of Technology

November 21, 2022

Abstract

Deep low-frequency earthquakes (LFEs) in Northeast Japan occur beneath active volcanoes at depths of 20-40 km. LFEs radiate low-frequency seismic waves, with most energy at 2-8 Hz, despite their low magnitudes (M $<$ 2). Although many previous studies have obtained various focal mechanisms with non-double-couple components and suggested physical processes related to magma, the universal physical process is poorly understood. Therefore, we comprehensively determined the focal mechanisms of 264 LFEs for 26 volcanic regions in Northeast Japan using S/P amplitude ratios. Many of the obtained solutions have large double-couple components with small compensated linear vector dipole components. Such source mechanisms can be explained by shear slip on the bending fault. We also find that the plunge of the null axis is as small as 20-30º at depths of 15-25 km, whereas it becomes larger and more various at deeper depths. We interpret that the regional stress field is relatively homogeneous in the middle of the crust, whereas it may be altered near the Moho discontinuity by thermal stress or other effects related to potential magmatic process. In addition, we quantitatively investigated the possible triggering of LFEs due to static stress change of both the 2008 Iwate-Miyagi earthquake and the 2011 Tohoku earthquake. The weak correlation between triggering potentials and activity change suggests that the activity of LFEs is more or less sensitive to temporal stress changes.

Depth Dependent Focal Mechanisms of Volcanic Deep Low-Frequency Earthquakes in Northeast Japan

Genki Oikawa[1], Naofumi Aso[1], and Junichi Nakajima[1]

[1] Department of Earth and Planetary Sciences, School of Science, Tokyo Institute of Technology, Tokyo, Japan

Corresponding author: Genki Oikawa (oikawa.g.aa@m.titech.ac.jp)

Key Points:

- Many of the obtained 264 focal mechanisms of deep low-frequency earthquakes in 26 regions have large double-couple components.
- The plunge of the null axis is as small as 20–30º at 15–25 km, whereas it becomes larger and more diverse at deeper depths.
- The triggering potential of large earthquakes correlate with the activity change of deep low-frequency earthquakes.

Abstract

Deep low-frequency earthquakes (LFEs) in Northeast Japan occur beneath active volcanoes at depths of 20–40 km. LFEs radiate low-frequency seismic waves, with most energy at 2–8 Hz, despite their low magnitudes (M < 2). Although many previous studies have obtained various focal mechanisms with non-double-couple components and suggested physical processes related to magma, the universal physical process is poorly understood. Therefore, we comprehensively determined the focal mechanisms of 264 LFEs for 26 volcanic regions in Northeast Japan using *S/P* amplitude ratios. Many of the obtained solutions have large double-couple components with small compensated linear vector dipole components. Such source mechanisms can be explained by shear slip on the bending fault. We also find that the plunge of the null axis is as small as 20–30º at depths of 15–25 km, whereas it becomes larger and more various at deeper depths. We interpret that the regional stress field is relatively homogeneous in the middle of the crust, whereas it may be altered near the Moho discontinuity by thermal stress or other effects related to potential magmatic process. In addition, we quantitatively investigated the possible triggering of LFEs due to static stress change of both the 2008 Iwate-Miyagi earthquake and the 2011 Tohoku earthquake. The weak correlation between triggering potentials and activity change suggests that the activity of LFEs is more or less sensitive to temporal stress changes.

Plain Language Summary

Deep slow earthquakes occurring near active volcanoes are thought to be related to deep magmatism. However, their physical processes are not well understood because of poor observations. In this study, to reveal their universal processes, we determined the focal mechanisms of 264 events for 26 volcanic regions in Northeast Japan, where deep slow earthquakes occur actively, and high-quality waveform data are available. Many of the obtained 264 focal mechanisms are dominated by shear slip components, similar to ordinary earthquakes. We find that the focal mechanisms of shallower events (< 25 km) are consistent with the regional stress field in Northeast Japan, while those of deeper events (> 25 km) are various. Such a disturbance of the stress field at a deeper depth may be generated by stagnated magma near the Moho discontinuity. We also found that the activity of deep slow earthquakes was triggered by

stress changes induced by large earthquakes. Our results suggest that spatiotemporal stress variations in Northeast Japan cause diverse activities of deep slow earthquakes.

1 Introduction

Deep low-frequency earthquakes (LFEs) in Northeast Japan occur actively beneath active volcanoes at depths of 20–40 km (Hasegawa & Yamamoto, 1994; Okada & Hasegawa, 2000; Niu et al., 2018) (Figure 1). The LFEs radiate low-frequency seismic waves, with most energy at 2–8 Hz, despite their small magnitudes (M < 2) (Figure 2). The Japan Meteorological Agency (JMA) has distinguished LFEs in Japan from ordinary earthquakes since 1999. Such LFEs have been observed worldwide in the subduction zone (e.g., Obara, 2002; Shelly & Hardebeck, 2010) or beneath active volcanoes (e.g., Aki & Koyanagi, 1981; Hasegawa & Yamamoto, 1994; Nichols et al., 2011). In terms of rheology, plastic deformation is thought to dominate over brittle deformations at focal depths of LFEs (Hasegawa et al., 1991). Therefore, LFEs are considered to occur under specific conditions, such as high pore pressure or fluid movements.

Aso et al. (2013) classified LFEs into three types based on the characteristics of the waveform and the seismicity of LFEs: tectonic, volcanic, and semi-volcanic. Tectonic LFEs are distributed on worldwide plate interfaces, and high pore pressure originating from the dehydration of the subducting slab is thought to be responsible for enabling brittle fractures (Shelly et al., 2006). On the other hand, volcanic LFEs have been observed beneath many active volcanoes worldwide (e.g., Aki & Koyanagi, 1981; Ukawa & Ohtake, 1987; Nichols et al., 2011). They are often distributed at the edge of the *S*-wave low-velocity zone in many regions (Niu et al., 2018), suggesting that occurrences are related with fluid movement. Semi-volcanic LFEs that occur far from active volcanoes are considered similar to volcanic LFEs based on their seismicity (Aso et al., 2013). Although the movement of magma or crustal fluids may be responsible for the volcanic or semi-volcanic LFEs (Hasegawa et al., 1991; Hasegawa & Yamamoto, 1994; Vidale et al., 2014), thermal stress due to cooling of a magma body has also been proposed as a potential driving force of these events (Aso & Tsai, 2014). Another characteristic of (semi-)volcanic LFEs is monotonic seismograms, which might result from resonance or oscillating source time functions (Aso & Ide, 2014). While tectonic LFEs are known to exhibit shear slip on

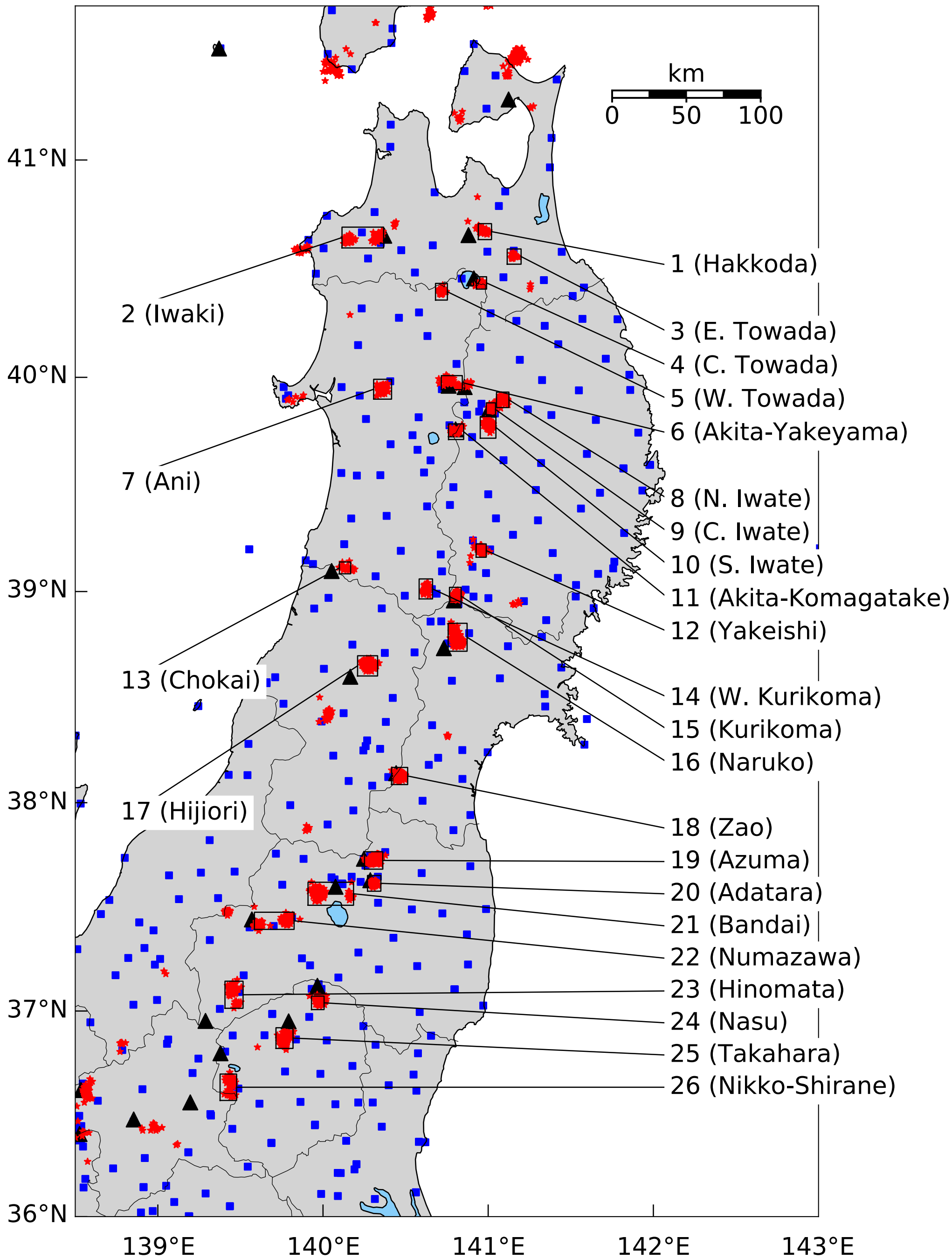

Figure 1. Hypocenter distribution of LFEs in Northeast Japan. Red dots indicate LFEs detected by the Japan Meteorological Agency (JMA) from January 2003 to December 2017. Black triangles represent active volcanoes. Blue squares denote permanent stations operated in Northeast Japan. The study areas are shown by black rectangles with subregion numbers.

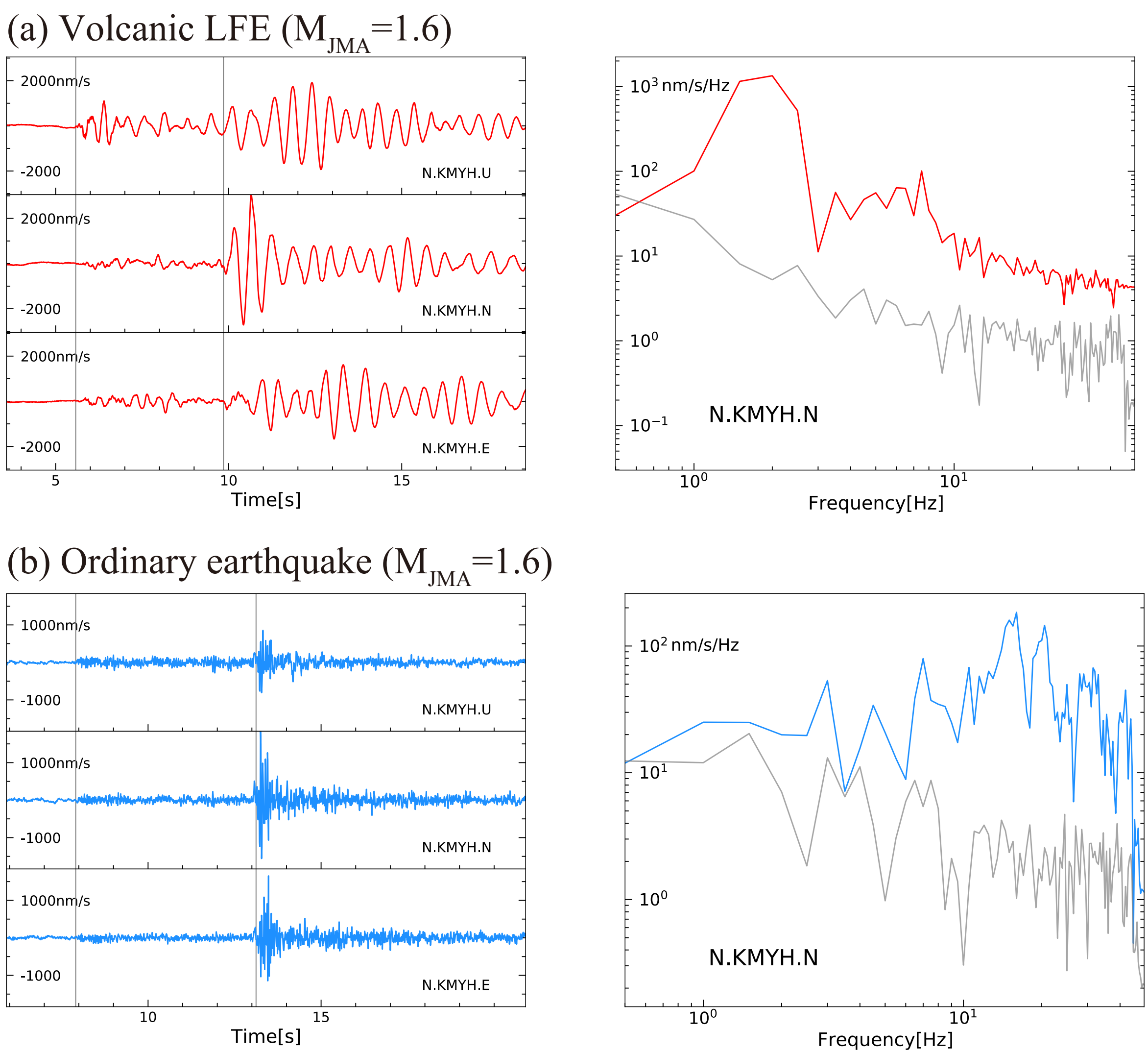

Figure 2. Representative waveform of volcanic LFE and ordinary earthquake. In each left panel, the three-component velocity waveforms recorded at station N.KMYH are shown by color lines, and vertical gray lines indicate *P*- and *S*-wave arrival times. In each right panel, the amplitude spectral density for the velocity waveform for the north-south component within 2 s from *S*-wave arrival is shown, and a gray line denotes the pre-event background spectrum. (a) The volcanic LFE with local magnitude M_{JMA}=1.6 that occurred in Zao (Area_18) at 12:11:15 on February 12, 2010 (JST). (b) The ordinary earthquake with local magnitude M_{JMA}=1.6 that occurred in Miyagi at 04:02:20 on March 30, 2011 (JST).

plate interfaces (Ide et al., 2007), the universal focal mechanisms of volcanic and semi-volcanic LFEs are poorly understood.

Understanding the (semi-)volcanic LFEs, especially concerning magmas or fluids, requires determining the focal mechanism of LFEs. Because the *P*-wave first motion of LFEs is unclear, the *S/P* amplitude ratio and waveform inversion technique are usually used for determining the mechanism. Previous studies have identified a variety of focal mechanisms, including double-couple, compensated linear vector dipole (CLVD), and isotropic components (Ukawa & Ohtake, 1987; Nishidomi & Takeo, 1996; Okada & Hasegawa, 2000; Ohmi & Obara, 2002; Nakamichi et al., 2003; Aso & Ide, 2014; Oikawa et al., 2019; Hensch et al., 2019). Non-double-couple (non-DC) mechanisms have also been found around volcanic regions or geothermal areas in the shallow part of the crust (e.g., Saraò et al., 2001; Foulger et al., 2004). Although LFEs are usually concentrated in a small cluster (Hasegawa & Yamamoto, 1994; Niu et al., 2018) and their mechanisms are expected to be uniform within the small cluster, diverse mechanisms have been obtained even within a narrow region (Nakamichi et al., 2003). Hence, LFEs may be caused by complex movements of faults, magma, and fluids. A large catalog of reliable focal mechanisms is required to reveal the universal genesis of LFEs.

Static stress triggering is another important factor in determining the source process of LFEs. For example, the 2011 Tohoku earthquake (Mw9.0) influenced the seismicity of shallow earthquakes over the Japanese Islands (Hirose et al., 2011), and previous studies have investigated between the activation of seismicity and the stress change due to the Tohoku earthquake. The increased number of inland earthquakes in the Iwaki region can be explained by local stress changes (Yoshida et al., 2012). Since its amplitude of the stress change is estimated to be as small as 1 MPa, a small initial differential stress is expected in this region. We also observed activated seismicity even in the negative ΔCFF region, which might be related to the change in the fluid pressure (Terakawa et al., 2013). Similar to ordinary earthquakes, it is reported that LFEs seem to be activated after large- to moderate-size of inland events (Hasegawa & Yamamoto, 1994) and that the Tohoku earthquake on the plate interface also influenced the seismicity of LFEs in the Tohoku region (Kosuga et al., 2017; Oikawa et al., 2019). To understand the activation mechanism of LFEs, we need to quantitatively compare the induced stress change and the seismicity change, using the large number of reliable focal mechanisms of LFEs.

For these purposes, we first determined the focal mechanisms of volcanic LFEs in 26 regions beneath Northeast Japan, where LFEs occur frequently, and high-quality seismographs are available owing to the high-density seismic observation network (Figure 1; Table 1). We then investigated the obtained focal mechanisms to constrain the physical processes of the LFEs. Finally, we investigated the static triggering of LFEs by regional earthquakes using the information on focal mechanisms.

No.	Region Name	Location		Average depth	Analyzed	Reliable
		Longitude[º]	Latitude[º]	[km]	LFEs	LFEs
1	Hakkoda	140.9717	40.6778	23.6	4	2
2	Iwaki	140.2680	40.6437	24.5	9	3
3	East Towada (E. Towada)	141.1547	40.5607	41.8	5	3
4	Central Towada (C. Towada)	140.953	40.4329	27.3	5	4
5	West Towada (W. Towada)	140.7174	40.3972	20.3	13	7
6	Akita-Yakeyama	140.7632	39.9832	19.9	4	3
7	Ani	140.3557	39.9471	31.0	32	19
8	North Iwate (N. Iwate)	141.0895	39.8964	34.2	9	5
9	Central Iwate (C. Iwate)	141.0184	39.8542	10.3	6	2
10	South Iwate (S. Iwate)	141.0010	39.7796	32.1	32	17
11	Akita-Komagatake	140.8033	39.7522	26.4	4	2
12	Yakeishi	140.9582	39.1931	32.1	11	3
13	Chokai	140.1315	39.1116	34.0	2	1
14	West Kurikoma (W. Kurikoma)	140.6237	39.0164	20.7	11	8
15	Kurikoma	140.8031	38.9782	19.4	17	9
16	Naruko	140.8137	38.7742	24.3	66	31
17	Hijiori	140.2708	38.6591	23.8	26	14
18	Zao	140.4678	38.1279	24.8	76	46
19	Azuma	140.3047	37.7289	28.0	46	22
20	Adatara	140.3091	37.6137	17.1	19	8
21	Bandai	139.9857	37.5691	30.6	20	12
22	Numazawa	139.7275	37.4301	25.9	19	16
23	Hinomata	139.4568	37.0897	29.6	15	6
24	Nasu	139.9746	37.0461	32.3	8	2
25	Takahara	139.7639	36.8593	24.3	29	15
26	Nikko-Shirane	139.4402	36.6563	30.3	13	4

Table 1. List of 26 regions showing location, average depth, the number of analyzed events, and that of events with reliable solution.

2 Data

The present study comprehensively analyzed the focal mechanisms of LFEs in 26 regions (Table 1). Based on the JMA catalog from January 2003 to December 2017, we focused on LFEs with local magnitudes $M_{JMA} \geq 0.5$. We used permanent stations located at epicentral distances of < 100 km with a sampling frequency of 100 Hz, operated by NIED (Hi-net), JMA, the University of Tokyo, Tohoku University, and Hirosaki University. We use stations with the information of *P* and *S* arrivals provided by JMA while we confirm all arrival times and reexamine several arrivals manually. We require signal-to-noise (S/N) ratios of ≥ 2.0 for both *P* and *S* waves, which are given by the ratios of the mean-square amplitudes between 2.0 s time windows before and after the arrivals. In this study, we analyzed 501 events for which six or more stations were available.

To estimate local site effects at each station, we also analyzed ordinary earthquakes of $2.0 \leq \mathrm{M_{JMA}} \leq 4.5$ at depths shallower than 150 km with known focal mechanisms (Figure S1). They consist of 2,774 events determined by the JMA and 1,934 events determined by Tohoku University (Data S1). We select their seismograms in the same manner as for LFEs, but we require S/N ratios of ≥ 3 for the reference ordinary events.

3 Methods

3.1 Focal mechanism determination

It is difficult to use unclear *P*-wave first motions of LFEs to estimate their focal mechanisms, whereas waveform inversion requires accurate seismic velocity structures. Therefore, in this study, we used the *S*/*P* amplitude ratio to determine the focal mechanisms of LFEs. We constrained nodal planes using the *S*/*P* amplitude ratio, as this method is advantageous when estimating the focal mechanisms of small earthquakes with low S/N ratios (Hardeback & Shearer, 2003). The use of amplitude ratios, rather than *S* or *P* wave absolute amplitudes, reduces errors caused by wave-propagation effects, such as geometric spreading (e.g., Foulger et al., 2004). Although the *S*/*P* amplitude ratio for low-S/N waveforms tends to introduce apparent bias in focal mechanisms, synthetic tests confirm that we can distinguish double-couple events and CLVD events (Text S1; Figure S2).

S/*P* amplitude ratios were calculated using three-component velocity seismograms at each station after applying a 1–15 Hz band-pass filter. We first determined the peak-to-peak amplitudes of the *P*-wave within 1 s of the *P*-wave arrival time: A_V^P and A_R^P for the vertical and radial components, respectively (Figure 3). Similarly, we determined the peak-to-peak amplitudes of the *S*-wave within 2 s of the *S*-wave arrival time: A_V^S, A_R^S, and A_T^S for vertical, radial, and transverse components, respectively (Figure 3). Considering that the amplitudes of *P* and *SV* waves vary depending on the incidence angle, we calculated the *S*/*P* ratios, defined as follows:

$$A^{obs} = \frac{\sqrt{(A_{SV})^2 + (A_{SH})^2}}{A_P} = \begin{cases} \dfrac{\sqrt{(A_R^S)^2 + (A_T^S)^2}}{A_V^P} & (\theta \leq 45°) \\ \dfrac{\sqrt{(A_V^S)^2 + (A_T^S)^2}}{A_R^P} & (\theta > 45°) \end{cases}, \quad (1)$$

where A_P, A_{SV}, and A_{SH} are the velocity amplitudes of the *P*, *SV*, and *SH* waves, respectively, and θ is the incidence angle. We use this formulation throughout the analysis, although this formulation is slightly different from the *S/P* amplitude ratio calculated using three-dimensional norms. We assume the observed *S/P* ratio of the *j*th event at the *i*th station as follows:

$$A_{ij}^{obs} = A_{ij}^{source} A_{ij}^{surf} A_{ij}^{site}, \quad (2)$$

where A_{ij}^{source} is estimated from the theoretical source radiation pattern, A_{ij}^{surf} is the free surface effect (Aki & Richards, 2002). A_{ij}^{site} includes local site effects and intrinsic attenuation along the ray path. The free surface effect A_{ij}^{surf} is theoretically calculated as a function of the incidence angle, assuming effective surface layer *P* and *S* wave velocities of 5.0 and 3.0 km/s, respectively. Take-off angles from sources and incidence angles to receivers were calculated by the ray-tracing method based on Zhao et al. (1992) using the JMA2001 velocity model (Ueno et al., 2001). Assuming that most attenuation occurs in the sedimentary layer near the receiver, the station corrections are assumed to be represented by three incident-angle-dependent values at each station: $A_{ij}^{site} = A_i^{site1}$ for incidence angles of ≦ 32°, $A_{ij}^{site} = A_i^{site2}$ for incidence angles of ≧ 32° and ≦ 45°, and $A_{ij}^{site} = A_i^{site3}$ for incidence angles ≧ 45°.

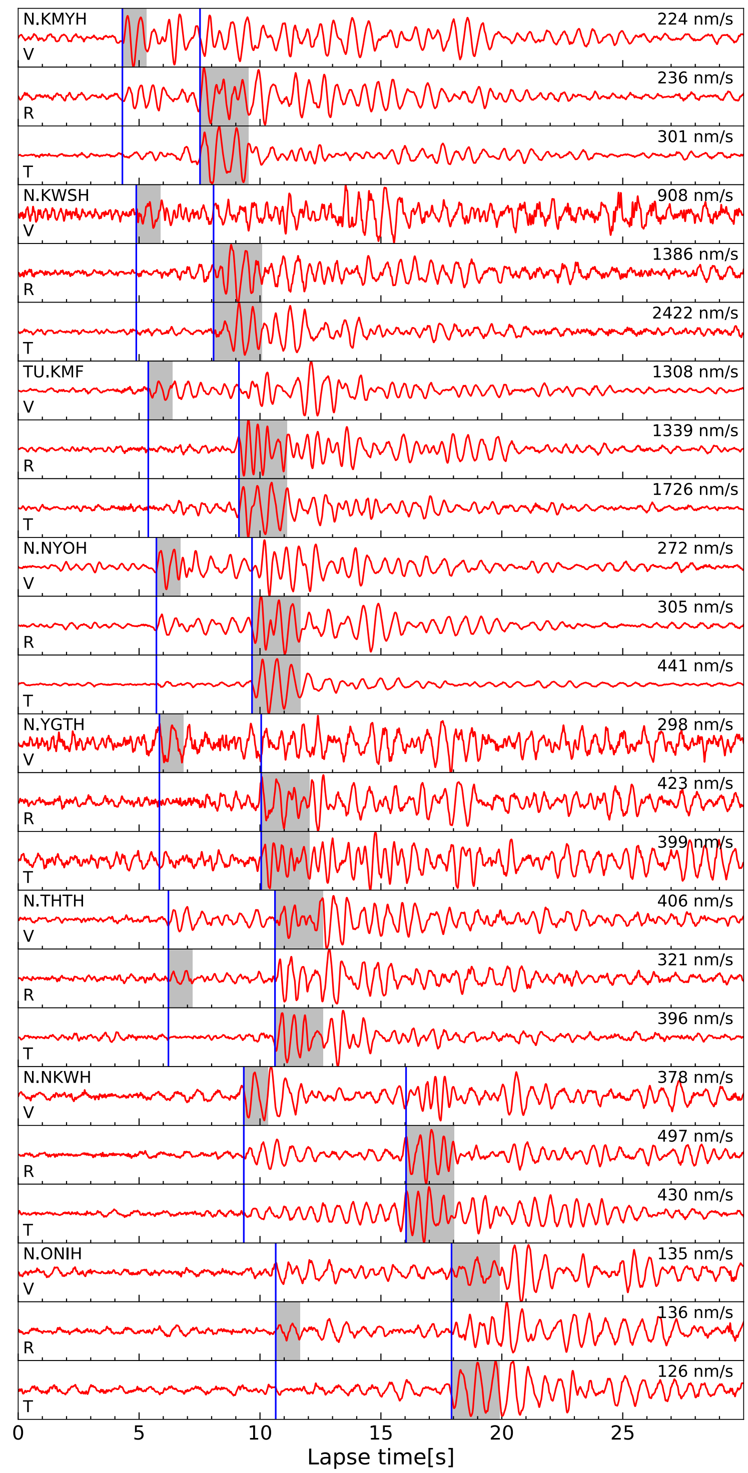

Figure 3. Example velocity waveforms of LFE in Zao (Area_18) that occurred at 22:12:41 on March 5, 2014 (JST). Each waveform is applied a 1–15 Hz band-pass filter. Vertical blue lines show *P*- and *S*- wave arrivals and the windows for the amplitude calculation are shown by gray shades. Each waveform is scaled by the maximum absolute amplitude shown in top-right.

$$A_{ij}^{site} = \begin{cases} A_i^{site1}\left(\theta_{ij} \le 32°\right), \\ A_i^{site2}\left(32° \le \theta_{ij} \le 45°\right) \\ A_i^{site3}\left(\theta_{ij} \ge 45°\right), \end{cases} \tag{3}$$

where θ_{ij} is the incidence angle of the *j*th event at the surface of the *i*th station.

We first estimated the site term using ordinary earthquakes with known focal mechanisms. By minimizing the logarithmic residual for the calibration events as follows:

$$\sum_{j \in EQ_{calib}} \left(\log_{10} A_{ij}^{obs} - \log_{10} A_{ij}^{source} - \log_{10} A_{ij}^{surf} - \log_{10} A_{ij}^{site}\right)^2 \to min\ , \tag{4}$$

we estimated parameters of A_i^{site1}, A_i^{site2}, and A_i^{site3}, which composes the site term A_{ij}^{site}. For each parameter, we required 15 or more available events. The obtained site terms A_i^{site1}, A_i^{site2}, and A_i^{site3} at each station are shown in Figure S3.

Once the calibration factors were determined, we estimated the focal mechanisms of the LFEs. By minimizing the logarithmic residual for each LFE as follows:

$$\sum_{i} \left(\log_{10} A_{ij}^{obs} - \log_{10} A_{ij}^{source} - \log_{10} A_{ij}^{surf} - \log_{10} A_{ij}^{site}\right)^2 \to min\ , \tag{5}$$

we estimated the moment tensor components of the LFEs, which comprise the source term A_{ij}^{source}. Generally, the moment tensor is a symmetric tensor with a total of six parameters, three eigenvalues, and three eigenvectors, but we reduce the parameters by adding two constraints of the moment tensor. First, we do not consider the isotropic component in this study because the volumetric part of the moment tensor has larger uncertainties than the deviatoric parts (Kawakatsu, 1996), and the large volumetric deformation is unlikely to occur at depths of 20–40 km. In addition, because the seismic moment of an earthquake cannot be determined by the *S/P* amplitude ratio, we do not consider the absolute value of the scalar moment. By these two constraints, we can reduce the number of parameters from six to four, including one for eigenvalues and three for eigenvectors. The one-dimensional grid search of eigenvalues is performed in the parameter space of $\tilde{\gamma}$ defined as:

$$\begin{bmatrix}\lambda_1\\ \lambda_2\\ \lambda_3\end{bmatrix} = \frac{2}{\sqrt{3}}\begin{bmatrix}\sin\left(\frac{\pi}{6}\tilde{\gamma}+\frac{\pi}{3}\right)\\ -\sin\left(\frac{\pi}{6}\tilde{\gamma}\right)\\ \sin\left(\frac{\pi}{6}\tilde{\gamma}-\frac{\pi}{3}\right)\end{bmatrix}, \qquad (6)$$

where $\lambda_1 > \lambda_2 > \lambda_3$ are the eigenvalues of the moment tensors. This formulation corresponds to the horizontal axis of a spherical cylindrical space (Aso et al., 2016), where the vertical axis is zero for no volumetric components. Although $\tilde{\gamma}$ generally takes values between ±1, we set the grid search range for $\tilde{\gamma}$ from 0–1.0 at intervals of 0.1. This range is set because we cannot distinguish opposite focal mechanisms from the *S/P* ratio patterns, which correspond to the same absolute amplitudes of $\tilde{\gamma}$ with opposite signs with the same set of eigenvectors. In general, the first eigenvector in 3-D space is represented by a strike angle within ±90º and a plunge angle within ±90º; the second eigenvector is represented by a rotational angle within ±90º, and the third eigenvector is given resultantly. Therefore, we set the grid search range for three angles from -90–90º at intervals of 5º. We note that the solution is given with an arbitrary sign because the two opposite focal mechanisms are not distinguishable from the *S/P* ratio.

3.2 Bootstrap test

To evaluate the stability of the obtained focal mechanisms, we performed the bootstrap test, in which the same number of samples (*S/P* ratios) used for mechanism analysis was selected in each trial, allowing duplicates. We conducted 100 trials of the bootstrap test for each event. An example of the bootstrap test in Zao (Area_18) is shown in Figure 4a. The stability of the solution is represented by the similarities between the nodal planes.

By extending the definition of the distance of moment tensors by Tape and Tape (2012), the distance between the nodal planes of the original solution ($\pm m^0$) and the bootstrap result ($\pm m$) can be evaluated as follows:

$$d(m^0, m) = 1 - \frac{\left|\sum_{pq} m_{pq}^0 m_{pq}\right|}{\sqrt{\sum_{pq}\left(m_{pq}^0\right)^2}\sqrt{\sum_{pq}\left(m_{pq}\right)^2}} \qquad (7)$$

(a)

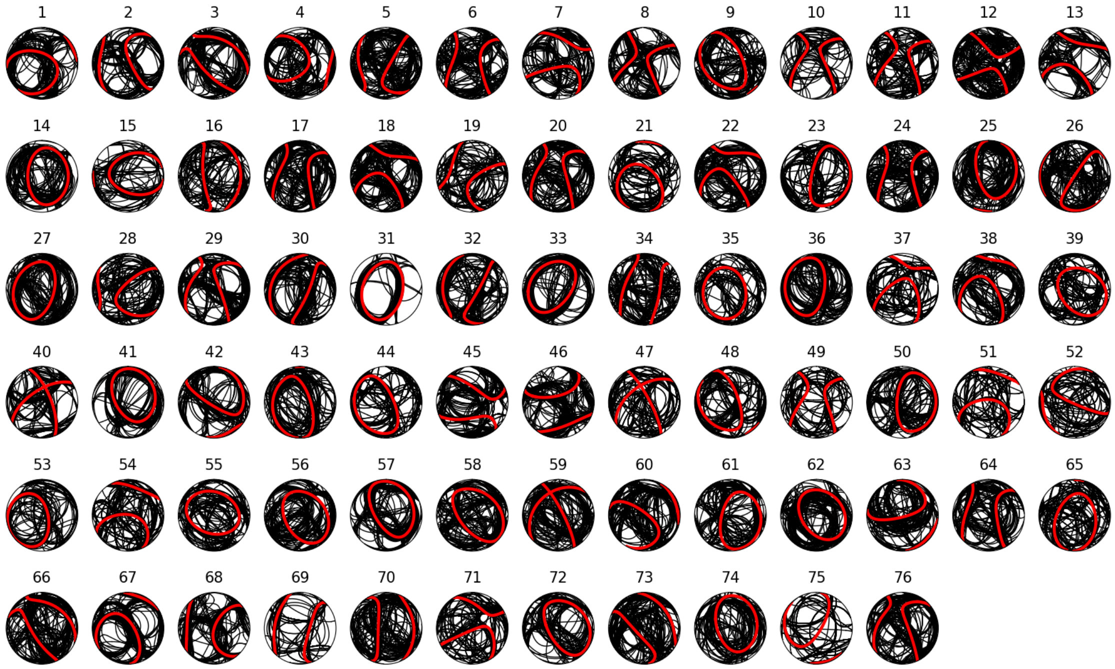

(b)

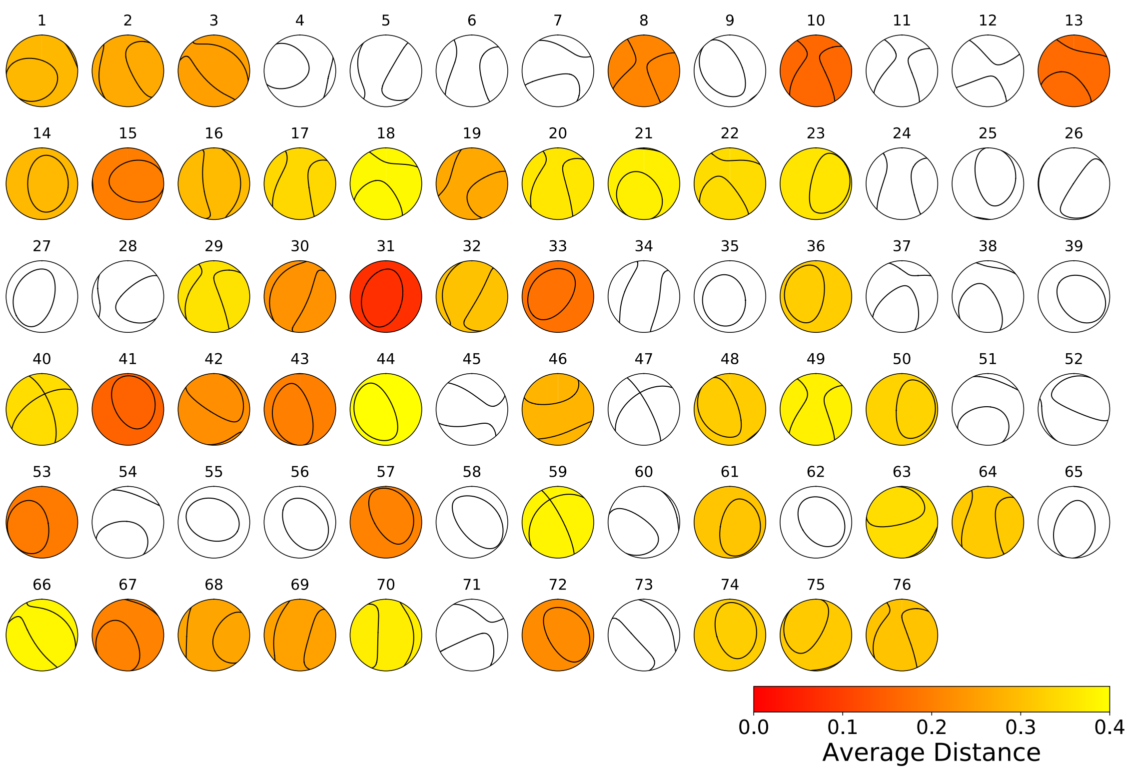

245

Figure 4. Bootstrap results in Zao. Mechanisms are plotted on lower hemisphere equal-area projections. Events are numbered in temporal order. (a) Obtained original focal mechanisms with bootstrap results. Red lines denote the nodal planes of original solutions. Black lines denote 100 bootstrap results. (b) Obtained original focal mechanisms colored by the average distance between original solutions and bootstrap test.

The distance takes values between 0–1, where two focal mechanisms sharing the same nodal planes result in $d = 0$.

We take an average value of d for 100 bootstrap iterations, which we call "average distance," to evaluate the stability of the original solution. For example, Events #10 and #31 in Zao, whose nodal planes do not vary significantly (Figure 4a), have a small average distance (Figure 4b). Based on this test, we regard LFEs with an average distance of less than 0.4, as the stable solutions. Numerical tests also support that average distances below this threshold correspond to statistically significant concentrations of nodal planes that cannot be explained by random distribution (Figure S4).

4 Obtained focal mechanism

Based on the bootstrap test, we selected 264 events with reliable solutions out of 501 analyzed events, and these events were used for discussion (Figure 5). The estimated moment tensor components for the 264 LFEs are summarized in Data S2. Although the principal axes of the obtained focal mechanisms vary among regions, several events in the same region share similar nodal planes (e.g., events #2, #3, and #4 in Ani; Area_7), suggesting the existence of a mature deformation system.

We find some events whose focal mechanisms are consistent with the regional stress field of Northeast Japan, which is east-west compression (Terakawa & Matsu'ura, 2010). For example, in Zao (Area_18), the obtained focal mechanisms such as #13, #17, and #46 are quite similar to the regional stress field. We also observed focal mechanisms with either P or T axes oriented in east-west direction in many regions. This result indicates that LFEs can be facilitated on the fault system developed by the regional stress, as we often observe for ordinary earthquakes in the upper crust.

One of the important findings in this study is that more than half of the obtained focal mechanisms in total have a large double-couple component (Figure 6). As we analyzed the initial part of the waveforms, this result suggests that the initial rupture process of LFEs is dominated by shear slip on the faults. However, there are a few events with large CLVD components (e.g., events #1, #5, and #7 in W. Towada), implying that the deformation is not always a slip on a flat fault surface. It is noted that the small number of pure double-couple events is apparent due to

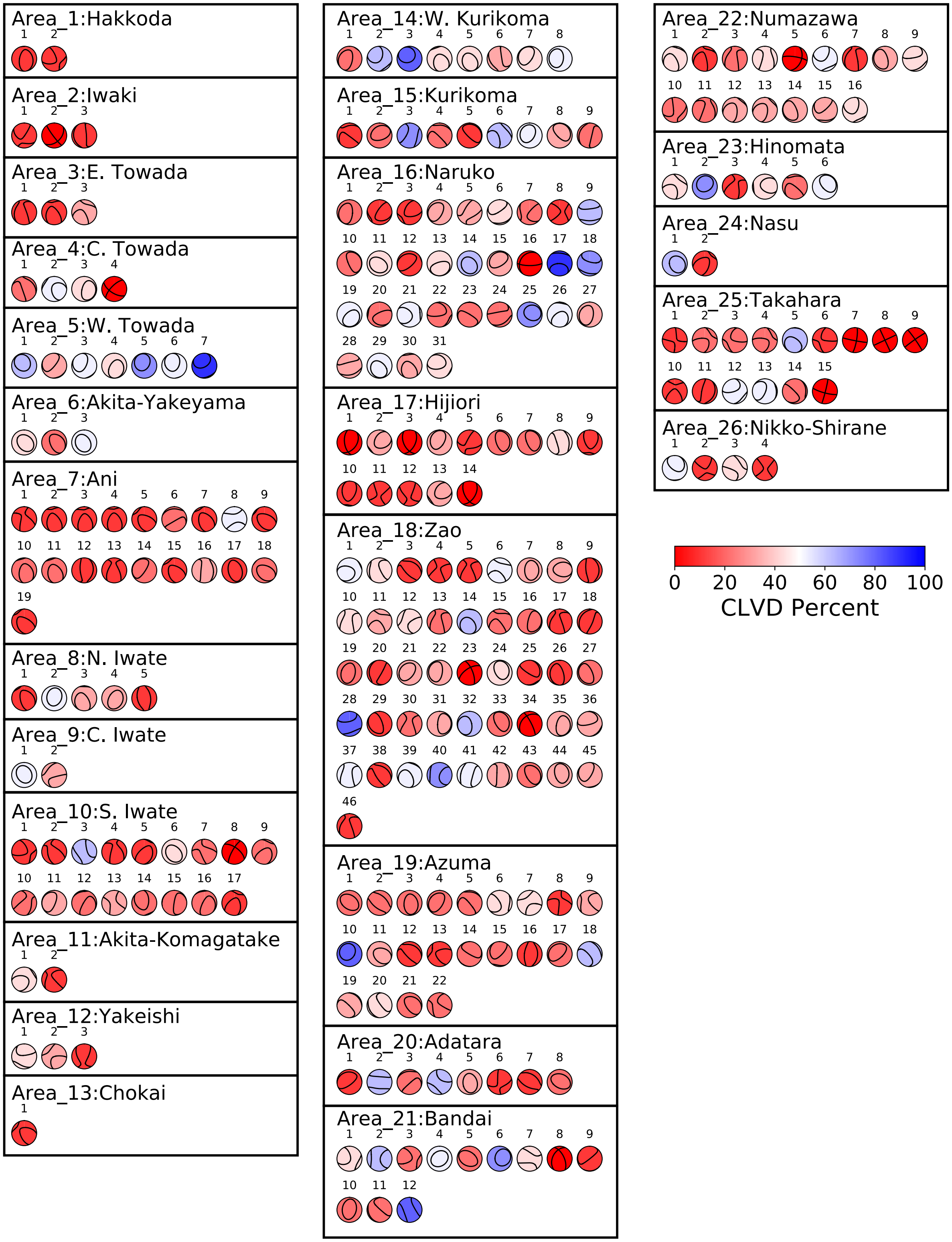
Area_1:Hakkoda
Area_2:Iwaki
Area_3:E. Towada
Area_4:C. Towada
Area_5:W. Towada
Area_6:Akita-Yakeyama
Area_7:Ani
Area_8:N. Iwate
Area_9:C. Iwate
Area_10:S. Iwate
Area_11:Akita-Komagatake
Area_12:Yakeishi
Area_13:Chokai
Area_14:W. Kurikoma
Area_15:Kurikoma
Area_16:Naruko
Area_17:Hijiori
Area_18:Zao
Area_19:Azuma
Area_20:Adatara
Area_21:Bandai
Area_22:Numazawa
Area_23:Hinomata
Area_24:Nasu
Area_25:Takahara
Area_26:Nikko-Shirane
0 20 40 60 80 100
CLVD Percent

Figure 5. Obtained focal mechanisms of 264 events in 26 regions with reliable solutions. Mechanisms are colored by the percentage of CLVD component $\frac{2|\lambda_2|}{\max(|\lambda_1|,|\lambda_3|)}$, where $\lambda_1 > \lambda_2 > \lambda_3$ are eigenvalues of the moment tensors.

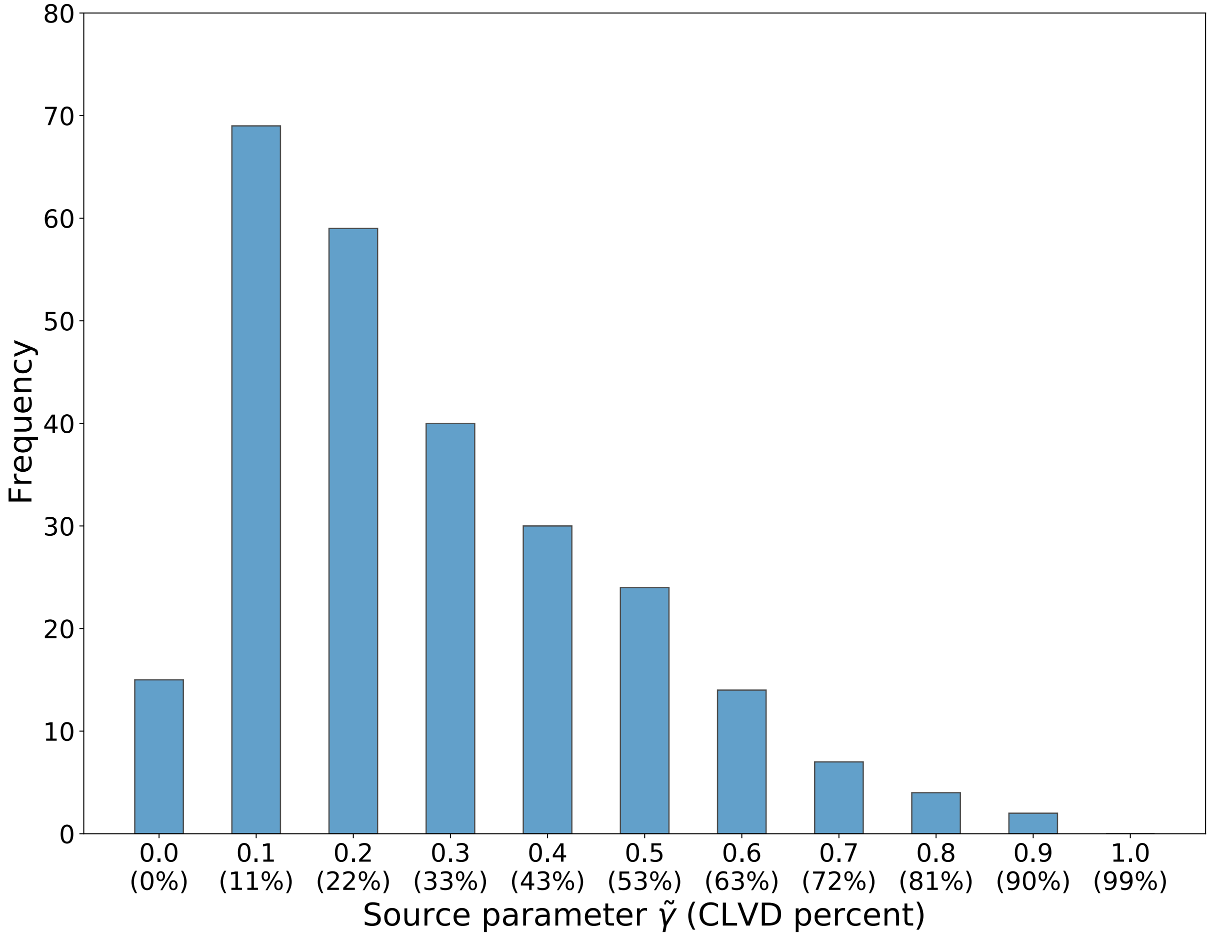

Figure 6. Frequency distribution of the source parameter (**$\tilde{\gamma}$**) of the obtained focal mechanisms for 264 events. Values in parentheses indicate the percentage of CLVD component.

the analysis method used in this study, but dominance of double-couple-like events is a robust result (Text S1; Figure S2).

We also find an interesting feature that the plunge angle of the null axis of focal mechanisms changes with depth. The plunge of the null axis is as small as 20–30º at depths of 15–25 km, whereas it becomes larger and more diverse at deeper depths, implying that shallower events tend to have more horizontal null axes by dip-slip fault movements (Figure 7). The rotation of the null axis is observed even within the same area, such as Zao, Hijiori, or Takahara (Figure S5). Our observations suggest that the stress state has large transitions throughout the lower crust between the Conrad and Moho discontinuities, which are estimated to be approximately 20 km and 35 km depths in Northeast Japan, respectively (Katsumata 2010). The genesis of the mechanism variations in the depth direction is discussed in Section 6.1.

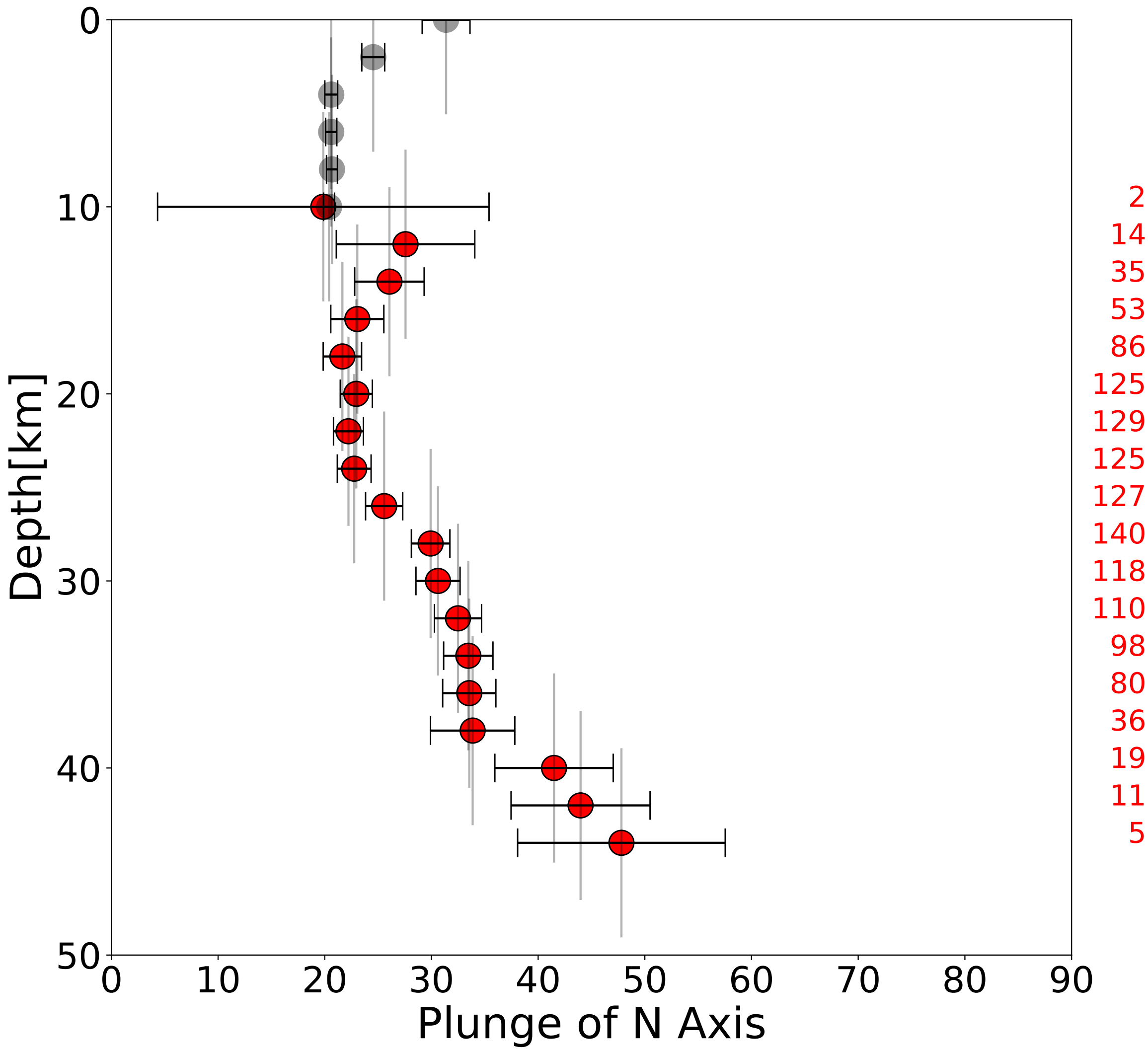

Figure 7. Plunge of the null axis as a function of depth. The red dots and horizontal lines indicate average and standard deviation (1σ) of the plunge, respectively, for LFEs over a range of 10 km every 2 km, which is shown by vertical lines. Those for shallow ordinary earthquakes used as calibration events are shown in grey. Rightmost numbers indicate the numbers of LFEs used for calculation in each bin.

5 Relationship between activity change and focal mechanisms of LFEs

LFEs in some regions show remarkable increases in seismicity after the Tohoku earthquake (Kosuga et al., 2017). However, it is difficult to evaluate the triggering potential strictly because we have only constrained the nodal planes of the focal mechanisms without polarity information. Therefore, we approximate the triggering potential, as described in Section 5.2, based on several assumptions, and we investigate the possible triggering of LFEs by both the 2008 Iwate-Miyagi earthquake the 2011 Tohoku earthquake.

5.1 Induced static stress

To evaluate the triggering potential, we first estimate induced stress tensors from slip on finite faults using the "Coulomb 3.3" program (Toda et al., 2005; Lin et al., 2004), based on analytical solutions of Okada (1992). For the Iwate-Miyagi earthquake, we used two rectangular faults modeled by Ohta et al. (2008). For the Tohoku earthquake, we considered both the mainshock and afterslip. As a fault model of the mainshock, we adopted the slip distribution of Ozawa et al. (2011), which was estimated using GNSS data. For the afterslip distribution, we amplified the results of Ozawa et al. (2011) by a factor of 9.4 as an estimation of the cumulative amount at the end of 2017. This extrapolation assumes that the spatial pattern of afterslip does not change over time, and we estimate the constant using the average geodetic displacements in the Tohoku region (Figure S6). The afterslip magnitude becomes Mw 8.9, consistent with the previous estimate of Mw 8.8 by Diao et al. (2014).

While the effect of the Iwate-Miyagi earthquake is limited to local areas such as Naruko, Kurikoma, and W. Kurikoma (Figure 8a), the Tohoku earthquake affected the entire Tohoku region because of its large extent of a fault length. The estimated pattern of stress tensors induced by the Tohoku earthquake and its afterslip is an east-west tension (Figure 8b), as shown in previous studies (Yoshida et al., 2012; Terakawa et al., 2013). We note that the effect of the afterslip is almost comparable to that of the mainshock (Figure S7).

5.2 Triggering potential

In general, both stress states before and after the triggering event, as well as representative focal mechanisms of potentially triggered events, are required to evaluate the

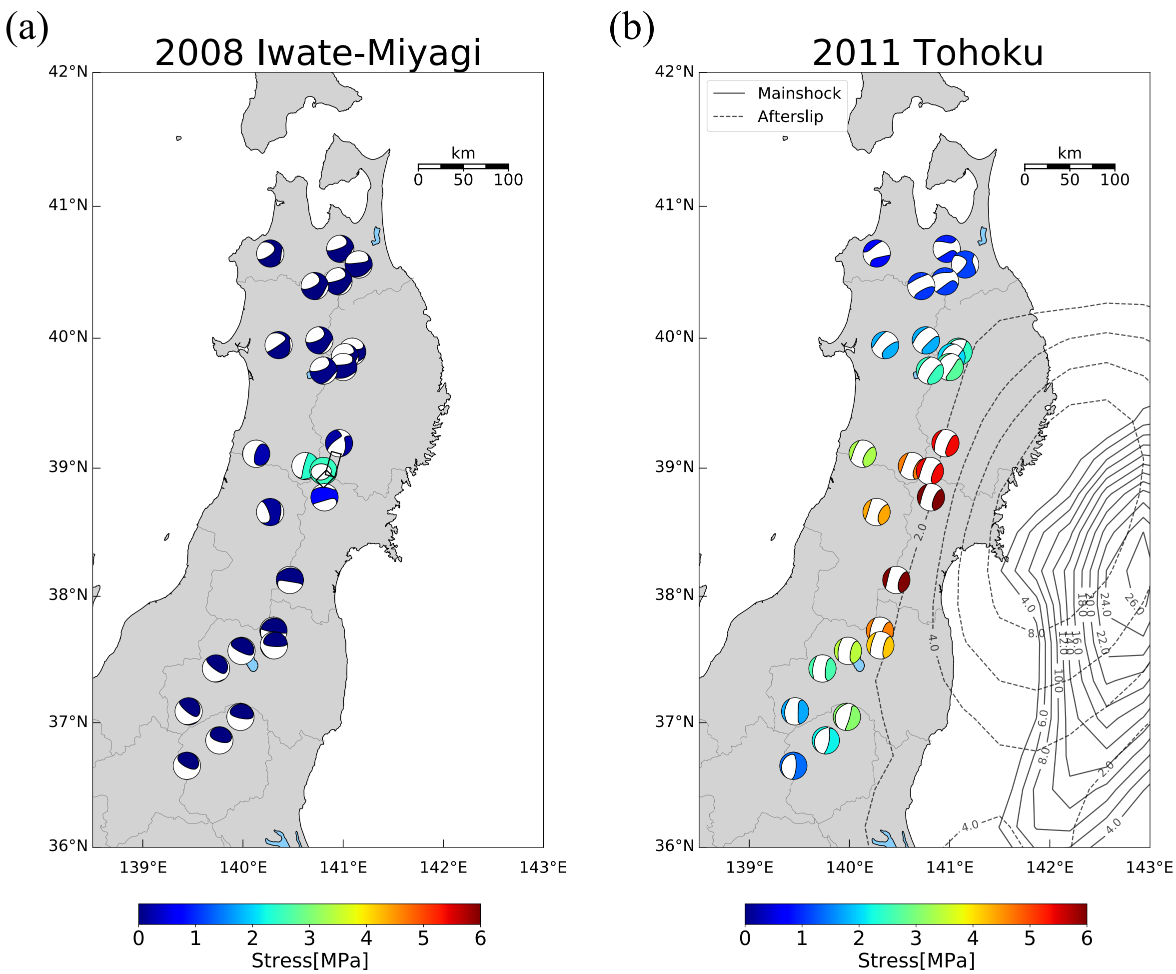

Figure 8. Distribution of stress tensors calculated for (a) the 2008 Iwate-Miyagi earthquake and (b) the 2011 Tohoku earthquake and its afterslip. Each beach ball is colored by the absolute value of induced stress at each area. The 2008 Iwate-Miyagi earthquake is modeled by two fault planes represented by black rectangles. The model of the 2011 Tohoku earthquake and its afterslip are represented by black contours at every 2 m.

triggering potential of large earthquakes. However, it is difficult to collect all of the information. Usually, 1) we do not know the absolute value of the background stress before the triggering events. In addition, in this study, 2) the focal mechanisms, which are required for calculating triggering potentials, are not necessarily unique in each area, and 3) we constrained only the nodal planes without polarities. Therefore, we need to make the following assumptions to evaluate the triggering potential:

A) We only considered the induced stress without knowledge of the background absolute stress level; this is the same assumption as that used for traditional approach of the Coulomb failure function (ΔCFF).

B) Focal mechanisms of events both before and after the triggering events are considered to represent common deformation style of LFEs. Based on this assumption, average of different triggering potentials calculated for different focal mechanisms are to represent triggering potential in each area. The time period was set to be from 2007-6-14 to 2009-6-14 for the Iwate-Miyagi earthquake and from 2009-6-14 to 2017-12-31 for the Tohoku earthquake.

C) Because we cannot distinguish the polarities of triggering potentials, we need to focus on unsigned triggering potentials. We considered the average value of unsigned triggering potentials in each area to evaluate whether the triggering effect is neutral or sensitive.

Based on the above assumptions, we made a rough estimation of the triggering potential. Generally, ΔCFF is used to assess the triggering potential of large earthquakes. However, it is not straightforward to extend the concept of the ΔCFF to evaluate the potential of triggering non-DC earthquakes, which are not necessarily frictional fault ruptures. Therefore, we instead evaluate the triggering potential for LFEs based on the similarities between the induced stress tensors σ and LFEs moment tensor m as follows:

$$1 - d(\sigma, m), \tag{8}$$

where d is the distance in the tensor orientations defined by Eq. (7), taking values between 0 and 1. Higher values correspond to the cases in which the moment tensor orientations of LFEs are similar to the orientations of induced stress, in which we expect large positive (activation) and negative (deactivation) triggering potential. However, small values of triggering potentials reflect a small potential for affecting the activity of LFEs. Because the estimated moment tensors of the

LFEs do not include the volumetric component, we consider only the deviatoric part of the stress tensors.

While we focused on induced stress orientations, its amplitude might also be an important factor. However, the contribution of the amplitude is rather complicated owing to the lack of knowledge on the in-situ background stress level; therefore, we focus only on the similarities in tensor orientations for simplicity.

5.3 Seismicity change after large events

We evaluate the temporal change of seismicity rate using the following equation:

$$\log_{10}\left(\frac{\mu_a}{\mu_b}\right), \tag{9}$$

where μ_b and μ_a are the seismicity rates of the LFEs before and after the triggering events, respectively. For the Iwate-Miyagi earthquake, μ_b is the seismicity from 2007-6-14 to 2008-6-14 and μ_a is that from 2008-6-14 to 2009-6-14. For the Tohoku earthquake, μ_b is the seismicity from 2009-6-14 to 2011-3-11, and μ_a is that from 2011-3-11 to 2017-12-31. Positive values indicate increased seismicity, zero means no activity change, and negative values correspond to quiescence. For the Iwate-Miyagi earthquake, the seismicity of LFEs around Kurikoma, where the absolute value of static stress is large (Figure 8a), seems to have changed slightly (Figure 9a). The seismicity of LFEs after the Tohoku earthquake has been active in a few regions, such as Zao, while it has decreased in most areas (Figure 9b).

5.4 Evaluation of static triggering

By comparing the activity change of LFEs with the estimated triggering potential, we investigate the causal relationship between these two factors. Although there is no clear trend between the two parameters, there seems to be characteristics between activity change and triggering potential. Specifically, there are no regions where the seismicity of LFEs has been altered, but the triggering potential is small (Figure 10). This weak correlation (R=0.43) indicates that stress tensor orientations act as necessary conditions for activity change, although it is not a sufficient condition. Of course, the background stress field and magnitude of the induced stress may have other important roles in the activity change. Otherwise, we notice that the similarities in orientations are a factor in trigger deciding. Based on the results, we conclude that not only ordinary earthquakes but also LFEs may be affected by static stress changes from local large earthquakes.

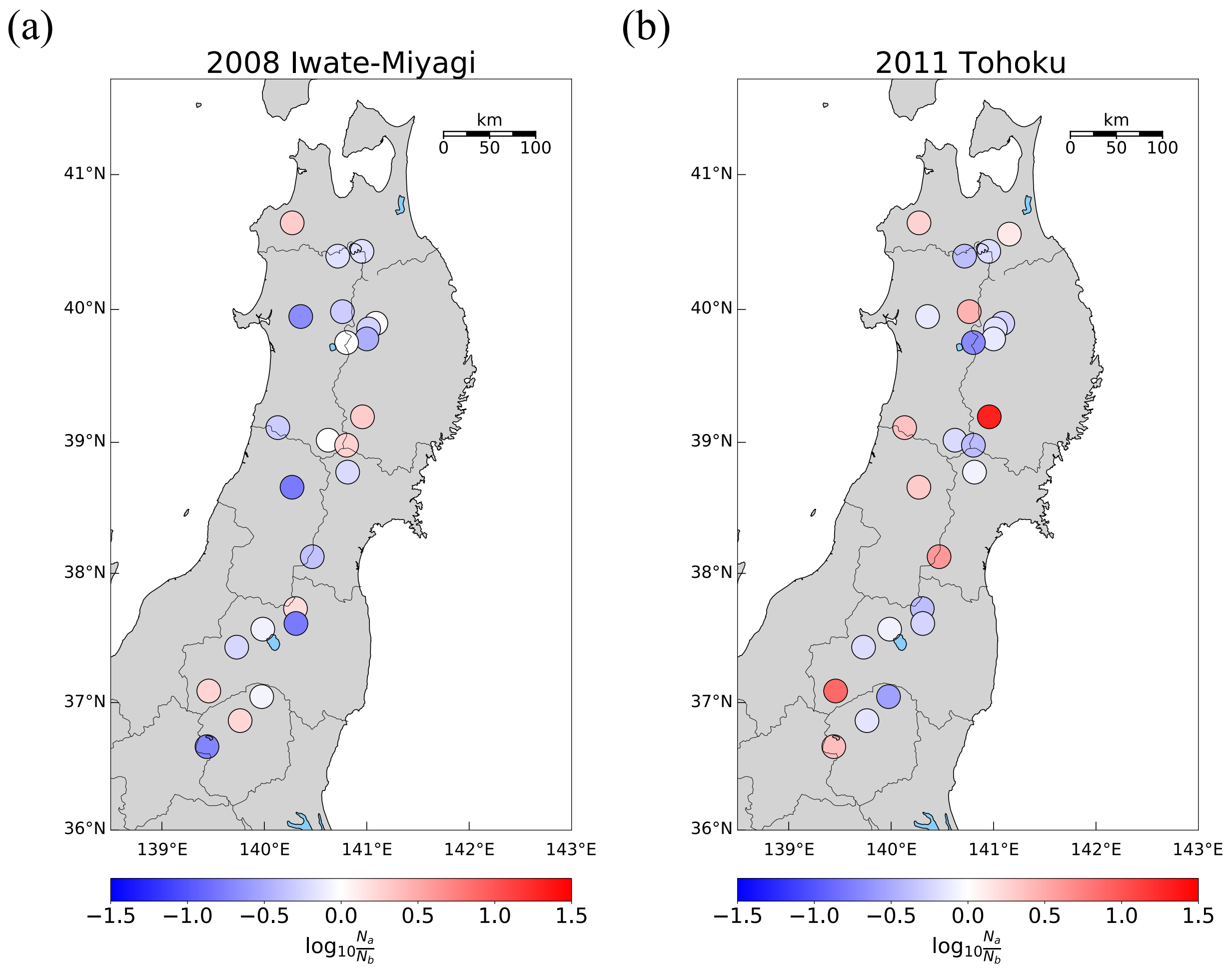

Figure 9. Calculated activity change in each area for (a) the 2008 Iwate-Miyagi earthquake. (b) the 2011 Tohoku earthquake. Regions colored by red indicates the number of LFEs have increased, white indicates no activity change, and blue colored dots mean deactivated areas.

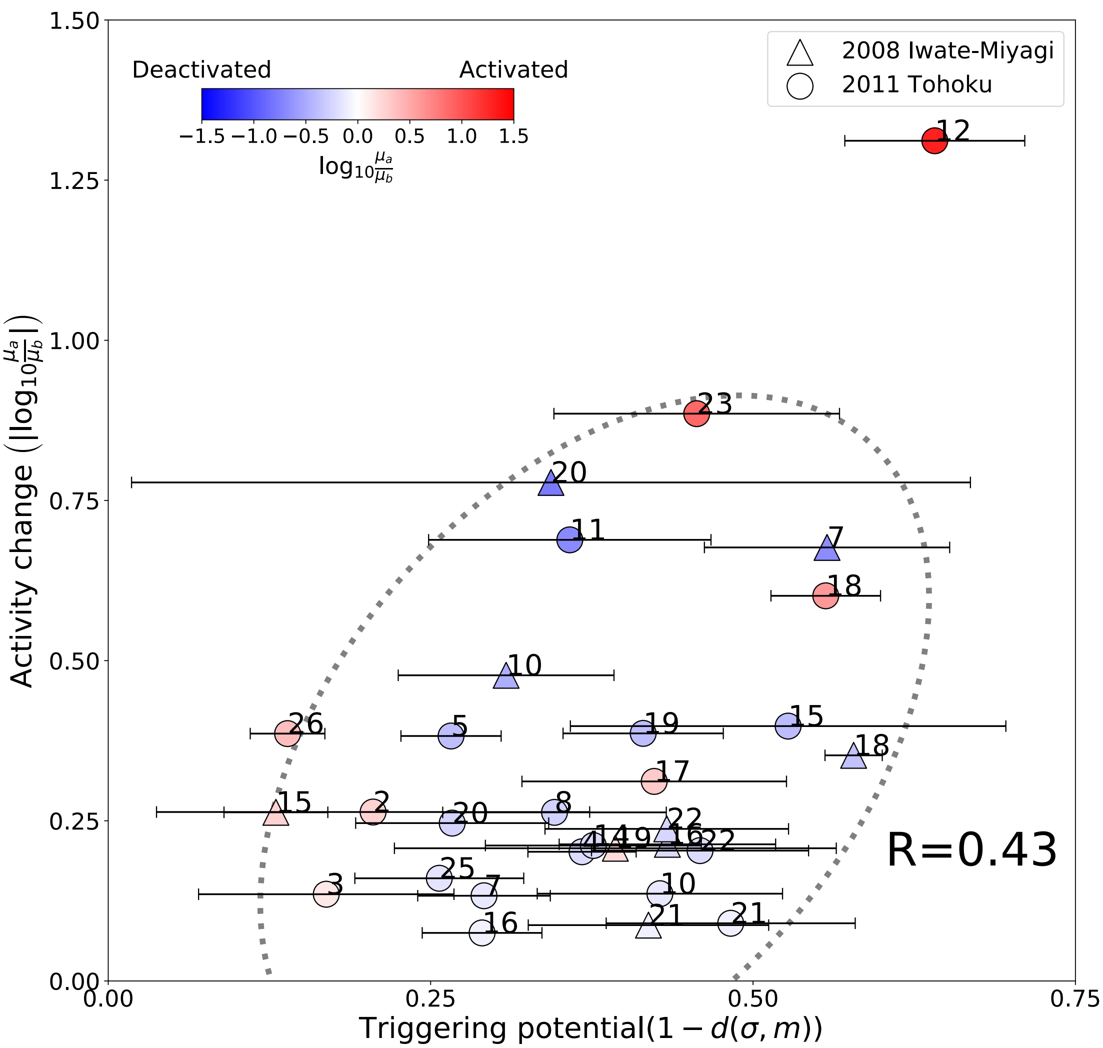

Figure 10. Relationship between activity change and triggering potential for the 2008 Iwate-Miyagi earthquake (triangle) and for the 2011 Tohoku earthquake (circle). The horizontal lines indicate standard deviations (1σ). The dotted oblique circle represents covariance matrix (2σ). Weak correlation is characterized by a correlation coefficient of R=0.43. There are no regions where the seismicity of LFEs have altered but the similarity is small (top-left area).

6 Discussion

6.1 Depth dependency on focal mechanisms of LFEs

The gradual rotation of the principal axes along the depth has been observed in various regions and depth ranges. Yoshida et al. (2015) found that the principal axis of shallow earthquakes in the Tohoku arc rotated following surface elevation. They also identified the rotation of the principal axes of shallow earthquakes occurring in the forearc region in the depth direction. Kato et al. (2011) reported that focal mechanisms drastically change from strike-slip to reverse faults in the 2–10 km depth range. While these studies focused on shallow ordinary earthquakes, we report the first case of principal-axis rotation for LFE events.

Depth-dependent stress rotation has been interpreted in two ways. The first candidate mechanism is associated with mechanical bending. Kato et al. (2011) proposed that the flexure of the upper crust causes depth-dependent horizontal stress. Yoshida et al. (2015) also interpreted forearc earthquakes with depth-dependent principal axes as the local stress caused by plate bending. However, plate bending does not affect the source region of the LFEs away from the plate interface. The other mechanism is related to depth-dependent lithostatic loading. Yoshida et al. (2015) suggested that the vertical lithostatic loading of topography causes heterogeneity in the stress field. Variations in the lateral force, Poisson's ratio, and viscosity may cause stress rotation to some extent at the local scale. However, no drastic stress rotation is inferred in Northeast Japan at a depth range of 20–40 km based on stress tensor inversion results (Terakawa & Matsu'ura, 2010). Hence, we need to consider another explanation for the rotation of the principal axes of LFEs with respect to depth.

Here, we interpret that the distinct rotation is due to the large variations in stress orientations near the Moho discontinuity. While our results for shallower LFEs (< 25 km) with dip-slip type are consistent with the regional stress field (Terakawa & Matsu'ura, 2010), the orientations of focal mechanisms are more various at deep depths, resulting in apparently large plunge of null axis in average (Figure 7). Hence, we consider that the disturbance of the regional stress field occurs at deep depths near the Moho discontinuity. One possible physical process of the disturbance is the deformation of the bi-material structures. Because the Moho discontinuity is a major material boundary, uniform tectonic contraction results in a heterogeneous stress field near the boundary. Another candidate is the stress disturbance associated with the heat transfer from magma. In addition to instantaneous stress disturbance due to magma intrusion, thermal stress would occur during the gradual cooling process of stagnated magma near the Moho discontinuity, which is proposed as a driving force of LFEs (Aso & Tsai, 2014). These processes may generate heterogeneous stress disturbances near the Moho discontinuity, explaining the variations in focal mechanisms near the Moho discontinuity compared to more uniform solutions at shallower depths.

6.2 Physical process of volcanic LFEs

Based on the focal mechanisms obtained in the present study, we discuss the universal coseismic deformation process of LFEs in this section. First, we considered three candidate physical processes to explain the obtained focal mechanisms. We then discuss the driving force of the LFEs to understand the mechanical process of the LFEs.

One candidate process is fluid movement. Shallow volcanic long period events and earthquakes associated with volcanic eruptions are often interpreted as fluid movements (e.g., Ohminato et al., 2006). In addition, the model of volcanic tremors excited by the non-linear motion of magma was suggested by Julian (1994). However, fluid movements cannot explain large double-couple components because the moment tensor of an earthquake caused by fluid flow in a cylindrical pipe is expected to be CLVD with a symmetry axis in the direction of flow. Therefore, we do not consider fluid movement as a predominant physical process of LFEs.

Physical processes associated with volume change are widely considered to explain non-DC earthquakes, including shallow and deep LFEs (e.g., Nakamichi et al., 2003). Even a pure volumetric change can result in a tensile crack and resultant shear movement influenced by local differential stress, known as a shear-tensile-crack model (Hill, 1977; Shimizu et al., 1987). This model radiates seismic waves by moving cracks and faults simultaneously when high-pressure fluid injection occurs. However, large volumetric deformation is unlikely to occur in deep-closed systems at the focal depth of the LFEs. In addition, volumetric deformation under deviatoric stress results in a large CLVD component, contradicting the majority of the obtained focal mechanisms with large double-couple components. Therefore, a shear-tensile-crack model is not suitable for a universal physical process of LFEs, although it may explain some of the LFEs.

Non-DC earthquakes can also be generated by non-planar faults without requiring volumetric changes (Dziewonski & Woodhouse, 1983; Ekström 1994; Shuler et al., 2013). Because the bending fault model is equivalent to the simultaneous shear slip on multiple faults with different azimuths, the apparent moment tensor has a CLVD component. Ekström (1994) calculated the moment tensor of ring faults, which is a type of bending fault, and showed that it could generate large CLVD earthquakes. The advantage of the bending fault model is its potential to explain various deviatoric deformations from double-couple to CLVD. Considering that this model does not require volumetric change, which may be difficult at the focal depth of LFEs, we claim that shear slip on the bending fault is our preference as a universal physical process of LFEs. In such bending faults, the complex fault structure may prevent efficient rupture growth, which explains the features of small magnitudes of LFEs.

While the bending fault model is a reasonable physical process accompanying seismic radiation based on the current knowledge, the background driving force producing deviatoric strain is more poorly understood. The cooling magma model was proposed as a physical process for localizing deformation near the Moho discontinuity around active or dormant volcanoes (Aso & Tsai, 2014). They showed that the large thermal stress generated by the stagnant magma around the Moho discontinuity causes shear failure. Recently, Wech et al. (2020) suggested that volatiles of stagnated cooling magma beneath the crust caused the LFE sequences beneath the Mauna Kea volcano. While the volatiles can be related to the deformation process by reducing the effective normal stress, they cannot be a direct driving force of LFEs because dynamic volumetric deformation is unlikely, as discussed. Instead, we propose thermal stress as the primary driving force of deep volcanic LFEs, consistent with heterogeneous stress conditions near the Moho discontinuity suggested by various focal mechanisms.

7 Conclusions

In the present study, we comprehensively determined the focal mechanisms of 264 volcanic LFEs in 26 regions beneath Northeast Japan using S/P amplitude ratios. Many of the obtained focal mechanisms have large double-couple components with small CLVD components, indicating that the initial rupture process of LFEs may be driven by shear slip. With regard to the deformation process of seismic radiation, CLVD components are probably excited as a result of shear slip along a bending fault.

Using the information of the obtained mechanisms, we find a weak correlation between the estimated triggering potentials of large earthquakes and the observed activity change. This relationship indicates that stress tensor orientations act as necessary conditions for activity change, although it is not a sufficient condition. Our results suggest that deep LFEs can be triggered by static stress change of local large earthquakes.

We also find that the plunge of the null axis is as small as 20–30º at 15–25 km, whereas it becomes larger and more diverse at deeper depths. While the null axis of LFEs at shallower depths is consistent with the regional stress field, the regional stress field is disturbed at deeper depths near the Moho discontinuity, which supports the contribution of thermal stress as a driving force of LFEs near the Moho discontinuity.

Data Availability Statement

Seismic waveform data can be downloaded from http://www.hinet.bosai.go.jp/?LANG=en (National Research Institute for Earth Science and Disaster Resilience, 2019). The hypocenters of LFEs determined by the JMA can be downloaded from https://www.data.jma.go.jp/svd/eqev/data/bulletin/hypo_e.html.

The source parameters (strike/dip/rake) of the earthquakes used for calibration of the local site effects are summarized in Data S1. The moment tensor components of the LFEs estimated in this study are listed in Data S2.

Acknowledgements

This work was supported by JSPS KAKENHI (JP21J10074, JP20K14576, JP19H04623, JP16H06475, and JP16H06477). The authors declare no conflict of interest.

References

Aki, K., & Richards, P. G. (2002). *Quantitative seismology*, (second ed.). Science Books, Sausalito, Calif: Univ.

Aki, K., & Koyanagi, R. (1981). Deep volcanic tremor and magma ascent mechanism under Kilauea, Hawaii. *Journal of Geophysical Research*, *86*(B8), 7095–7109. https://doi.org/10.1029/JB086iB08p07095

Aso, N., Ohta, K., & Ide, S. (2013). Tectonic, volcanic, and semi-volcanic deep low-frequency earthquakes in western Japan. *Tectonophysics*, *600*, 27–40. https://doi.org/10.1016/j.tecto.2012.12.015

Aso, N., & Ide, S. (2014). Focal mechanisms of deep low-frequency earthquakes in Eastern Shimane in Western Japan. *Journal of Geophysical Research*, *119*, 364–377. https://doi.org/10.1002/2013JB010681

Aso, N., & Tsai, V. C. (2014). Cooling magma model for deep volcanic long-period earthquakes. *Journal of Geophysical Research, 119*, 8442–8456. https://doi.org/10.1002/2014JB011180

Aso, N., & Ohta, K. & Ide, S. (2016), Mathematical review on source-type diagrams, *Earth Planet Space*, *68*(1), 52, doi:10.1186/s40623-016-0421-5. https://doi.org/10.1186/s40623-016-0421-5

Diao, F., Xiong, X., Wang, R., Zheng, Y., Walter, T. R., Weng, H., & Li, J. (2014). Overlapping postseismic deformation processes: Afterslip and viscoelastic relaxation following the 2011 Mw 9.0 Tohoku (Japan) earthquake. Geophysical Journal International, 196(1), 218–229. https://doi.org/10.1093/gji/ggt376

Dziewonski, A. M., & Woodhouse, J. H. (1983). An experiment in systematic study of global seismicity: Centroid-moment tensor solutions for 201 moderate and large earthquakes of 1981. *Journal of Geophysical Research, 88*, 3247–3271. https://doi.org/10.1029/JB088iB04p03247

Ekström, G. (1994). Anomalous earthquakes on volcano ring-fault structures. *Earth and Planetary Science Letters, 128*, 707–712. https://doi.org/10.1016/0012-821X(94)90184-8

Foulger, G. R., Julian, B. R., Hill, D. P., Pitt, A. M., Malin, P. E., & Shalev, E. (2004). Non-double-couple microearthquakes at Long Valley caldera, California, provide evidence for hydraulic fracturing. *Journal of Volcanology and Geothermal Research, 132*(1), 45-71. https://doi.org/10.1016/S0377-0273(03)00420-7

Han, J., Vidale, J. E., Houston, H., Schmidt, D. A., & Creager, K. C. (2018). Deep long-period earthquakes beneath Mount St. Helens: Their relationship to tidal stress, episodic tremor and slip, and regular earthquakes. *Geophysical Research Letters, 45*, 2241–2247. https://doi.org/10.1002/2018GL077063

Hardebeck, J. L., & Shearer, P. M. (2002). A new method for determining first- motion focal mechanisms. *Bulletin of the Seismological Society of America*, *92*(6), 2264-2276. https://doi.org/10.1785/0120010200

Hardebeck, J. L., & Shearer, P. M. (2003). Using S/P amplitude ratios to constrain the focal mechanisms of small earthquakes. *Bulletin of the Seismological Society of America, 93*(6), 2434–2444. https://doi.org/10.1785/0120020236

Hasegawa, A., Zhao, D., Hori, S., Yamamoto, A., & Horiuchi, S. (1991). Deep structure of the northeastern Japan arc and its relationship to seismic and volcanic activity. *Nature, 352*(6337), 683–689. https://doi.org/10.1038/352683a0

Hasegawa, A., & Yamamoto, A. (1994). Deep, low-frequency microearthquakes in or around seismic low-velocity zones beneath active volcanoes in northeastern Japan. *Tectonophysics, 233*(3-4), 233–252. https://doi.org/10.1016/0040-1951(94)90243-7

Hensch, M., Dahm, T., Ritter, J., Heimann, S., Schmidt, B., Stange, S., & Lehmann, K. (2019). Deep low-frequency earthquakes reveal ongoing magmatic recharge beneath Laacher See Volcano (Eifel, Germany). *Geophysical Journal International, 216*(3), 2025-2036. https://doi.org/10.1093/gji/ggy532

Hill, D. P. (1977). A model for earthquake swarms. *Journal of Geophysical Research, 82*(8), 1347–1352. https://doi.org/10.1029/JB082i008p01347

Hirose, F., Miyaoka, K., Hayashimoto, N., Yamazaki, T., & Nakamura, M. (2011). Outline of the 2011 off the Pacific coast of Tohoku earthquake (Mw 9.0)-Seismicity: Foreshocks, mainshock, aftershocks, and induced activity. *Earth, Planets and Space, 63*(7), 513–518. https://doi.org/10.5047/eps.2011.05.019.

Ide, S., Shelly, D. R., & Beroza, G. C. (2007). Mechanism of deep low frequency earthquakes: Further evidence that deep non-volcanic tremor is generated by shear slip on the plate interface. *Geophysical Research Letters, 34*, L03308. https://doi.org/10.1029/2006GL028890

Julian, B. (1994). Volcanic tremor: Nonlinear excitation by fluid flow. *Journal of Geophysical Research*, *99*, 11,859–11,877. https://doi.org/10.1029/93JB03129

Kato, A., et al. (2011), Anomalous depth dependency of the stress field in the 2007 Noto Hanto, Japan, earthquake: Potential involvement of a deep fluid reservoir, *Geophysical Research Letters*, *38*, L06306. https://doi.org/10.1029/2010GL046413.

Katsumata, A. (2010), Depth of the Moho discontinuity beneath the Japanese islands estimated by traveltime analysis, *Journal of Geophysical Research*, 115, B04303, 10.1029/2008JB005864.

Kawakatsu, H. (1996). Observability of the isotropic component of a moment tensor. *Geophysical Journal International*, *126*, 525–544. https://doi.org/10.1111/j.1365-246X.1996.tb05308.x

Kosuga, M., Noro, K., & Masukawa, K. (2017). Characteristics of spatiotemporal variations of hypocenters and diversity of waveforms of deep low-frequency earthquakes in northeastern Japan. *Bulletin. Earthquake Research Institute, University of Tokyo, 92*(2), 63–80. in Japanese with English abstract

Lin, J., & Stein, R. S. (2004). Stress triggering in thrust and subduction earthquakes and stress interaction between the southern San Andreas and nearby thrust and strike-slip faults. *Journal of Geophysical Research, 109*. https://doi.org/10.1029/2003JB002607

Nakamichi, H., Hamaguchi, H., Tanaka, S., Ueki, S., Nishimura, T., & Hasegawa, A. (2003). Source mechanisms of deep and intermediate-depth low-frequency earthquakes beneath Iwate volcano, northeastern Japan. *Geophysical Journal International, 154*(3), 811–828. https://doi.org/10.1046/j.1365-246X.2003.01991.x

Nichols, M. L., Malone, S. D., Moran, S. C., Thelen, W. A., & Vidale, J. E. (2011). Deep long-period earthquakes beneath Washington and Oregon volcanoes. *Journal of Volcanology and Geothermal Research, 200*(3-4), 116–128. https://doi.org/10.1016/j.jvolgeores.2010.12.005

Nishidomi, I., & Takeo, M. (1996). Seismicity and a focal mechanism of low-frequency earthquakes occurring in the western part of Tochigi prefecture, Japan. *Bulletin of the Volcanological Society of Japan, 41*, 43–59. (in Japanese with English abstract)

Niu, X., Zhao, D., & Li, J. (2018). Precise relocation of low-frequency earthquakes in northeast Japan: New insight into arc magma and fluids. *Geophysical Journal International, 212*(2), 1183–1200. https://doi.org/10.1093/gji/ggx445

Obara, K. (2002). Nonvolcanic deep tremor associated with subduction in southwest Japan. *Science, 296*(5573), 1679–1681. https://doi.org/10.1126/science.1070378

Oikawa, G., Aso, N., & Nakajima, J. (2019). Focal mechanisms of deep low-frequency earthquakes beneath Zao volcano, Northeast Japan, and relationship to the 2011 Tohoku earthquake. *Geophysical Research Letters, 46*. https://doi.org/10.1029/2019GL082577

Ohmi, S., & Obara, K. (2002). Deep low-frequency earthquakes beneath the focal region of the Mw 6.7 2000 western Tottori earthquake. *Geophysical Research Letters*, *29*(16), 1807. https://doi.org/10.1029/2001GL014469

Okada, Y. (1992). Internal deformation due to shear and tensile faults in a half-space. *Bulletin of the Seismological Society of America, 82*(2), 1018-1040.

Okada, T., & Hasegawa, A. (2000). Activity of deep low-frequency micro-earthquakes and their moment tensors in northeastern Japan. *Bulletin of the Volcanological Society of Japan*, *45*(2), 47–63. in Japanese with English abstract

Ohta, Y., Ohzono, M., Miura, S., Iinuma, T., Tachibana, K., Takatsuka, K., Miyao, K., Sato, T., & Umino, N. (2008), Coseismic fault model of the 2008 Iwate-Miyagi Nairiku earthquake deduced by a dense GPS network, *Earth Planets Space*, *60*, 1197–1201. https://doi.org/10.1186/BF03352878

Ohminato, T., Takeo, M., Kumagai, H., Yamashima, T., Oikawa, J., Etsuro, K., Tsuji, H., & Urabe, T. (2006), Vulcanian eruptions with dominant single force components observed during the Asama 2004 volcanic activity in Japan, *Earth Planets Space*, *58*, 583–593. https://doi.org/10.1186/BF03351955

Ozawa, S., Nishimura, T., Suito, H., Kobayashi, T., Tobita, M., & Imakiire, T. (2011). Coseismic and postseismic slip of the 2011 magnitude-9 Tohoku-Oki earthquake. *Nature*, *475*(7356), 373–376. https://doi.org/10.1038/nature10227

Saraò, A., Panza, G., Privitera, E., & Cocina, O. (2001). Non-double-couple mechanisms in the seismicity preceding the 1991-1993 Etna volcano eruption. *Geophysical Journal International, 145*(2), 319–335. https://doi.org/10.1046/j.1365-246X.2001.01375.x

Shelly, D. R., & Hardebeck, J. L. (2010). Precise tremor source locations and amplitude variations along the lower-crustal central San Andreas Fault. *Geophysical Research Letters*, *37*, L14301. https://doi.org/10.1029/2010GL043672

Shimizu, H., Ueki, S., & Koyama, J. (1987). A tensile-shear crack model for the mechanism of volcanic earthquakes. *Tectonophysics*,*144*(1-3), 287-300. https://doi.org/10.1016/0040-1951(87)90023-0

Shuler, A., Ekstroem, G., & Nettles, M. (2013). Physical mechanisms for vertical-CLVD earthquakes at active volcanoes. *Journal of Geophysical Research, 118*, 1569-1586. https://doi.org/10.1002/jgrb.50131

Tape, W., & Tape, C. (2012). Angle between principle axis triples. *Geophysical Journal International, 191*(2), 813–831. https://doi.org/10.1111/j.1365-246X.2012.05658.x

Terakawa, T., & Matsu'ura, M. (2010). The 3-D tectonic stress fields in and around Japan inverted from centroid moment tensor data of seismic events. *Tectonics*, *29*, TC6008. https://doi.org/10.1029/2009TC002626

Terakawa, T., Hashimoto, C., & Matsu'ura, M. (2013). Changes in seismic activity following the 2011 Tohoku-oki earthquake: Effects of pore fluid pressure. *Earth and Planetary Science Letters*, *365*, 17–24. https://doi.org/10.1016/j.epsl.2013.01.017

Toda, S., Stein, R. S., Richards-Dinger, K., & Bozkurt, S. B. (2005). Forecasting the evolution of seismicity in Southern California: Animations built on earthquake stress transfer. *Journal of Geophysical Research, 110*, B05S16. https://doi.org/10.1029/2004JB003415

Ueno, H., Hatakeyama, S., Aketagawa, T., Funasaki, J., & Hamada, N. (2002). Improvement of hypocenter determination procedures in the Japan Meteorological Agency (in Japanese with English abstract. *Quarterly Journal of Seismology*, *65*, 123–134.

Ukawa, M., & Ohtake, M. (1987). A monochromatic earthquake suggesting deep-seated magmatic activity beneath the Izu-Ooshima Volcano, *Japan. Journal of Geophysical Research*, *92*(B12), 12,649–12,663. https://doi.org/10.1029/JB092iB12p12649

Vidale, J. E., Schmidt, D. A., Malone, S. D., Hotovec-Ellis, A. J., Moran, S. C., Creager, K. C., & Houston, H. (2014). Deep long-period earthquakes west of the volcanic arc in Oregon: Evidence of serpentine dehydration in the fore-arc mantle wedge. *Geophysical Research Letters*, *41*, 370–376. https://doi.org/10.1002/2013GL059118

Yoshida, K., Hasegawa, A., Okada, T., Iinuma, T., Ito, Y., & Asano, Y. (2012). Stress before and after the 2011 great Tohoku-oki earthquake and induced earthquakes in inland areas of eastern Japan. *Geophysical Research Letters*, *39*, L03302. https://doi.org/10.1029/2011GL049729

Yoshida, K., Hasegawa, A., & Okada, T. (2015). Spatial variation of stress orientations in NE Japan revealed by dense seismic observations. *Tectonophysics*, *647-648*, 63-72. https://doi.org/10.1016/j.tecto.2015.02.013

Zhao, D., Hasegawa, A., & Horiuchi, S. (1992). Tomographic imaging of P and S wave velocity structure beneath northeastern Japan. *Journal of Geophysical Research, 97*(B13), 19,909-19,928. https://doi.org/10.1029/92JB00603

Journal of Geophysical Research: Solid Earth

Supporting Information for

Depth Dependent Focal Mechanisms of Volcanic Deep Low Frequency Earthquakes in Northeast Japan

Genki Oikawa[1], Naofumi Aso[1], and Junichi Nakajima[1]

[1] Department of Earth and Planetary Sciences, School of Science, Tokyo Institute of Technology, Tokyo, Japan

Contents of this file

Text S1
Figures S1 to S7

Additional Supporting Information (Files uploaded separately)

- **Data S1. (Separate file)**
  Data S1 contains the source parameters of earthquakes used for the estimation of local site effects.
- **Data S2. (Separate file)**
  Data S2 contains the moment tensor components of low-frequency earthquakes estimated in this study. Moment tensor components are expressed in the northeast-down system. The x-axis, y-axis, and z-axis correspond to north, east, and down, respectively.

Introduction

Text S1 describes the procedure for the synthetic test to validate our method. Figure S1 shows the hypocenter distributions of ordinary earthquakes used for station corrections. Figure S2 shows the obtained frequency distribution of the compensated linear vector dipole (CLVD) percent for the synthetic tests. Figure S3 shows the site terms obtained in this study. Figure S4 shows the validity of the bootstrap test threshold. Figure S5 shows the plunge angle of the null axis for 264 events as a function of depth. Figure S6 shows the station distribution of the global navigation satellite system (GNSS) used for extrapolation. Figure S7 shows the estimated stress tensors of both the mainshock and afterslip of the 2011 Tohoku earthquake.

■ Text S1. Validity test of CLVD percent distribution

To evaluate the validity of the obtained frequency distribution of CLVD percent (Figure 6), we conducted a synthetic test of mechanism determination using the same data set as for the analysis in this study. We calculated the synthetic waveforms of both ordinary earthquakes used for station correction and low-frequency earthquakes (LFEs) using the method of Zhu and Rivera (2002). The site amplification factor used for the synthetic test was the same as that used in this study (Figure S3). For LFEs, we perform a synthetic test for two patterns of focal mechanisms: pure double couple and CLVD. We assume a double-couple source with strike=0º, dip=45º, and rake=90º and CLVD with $(M_{xx}\,, M_{yy}\,, M_{zz}) = (-2\,, 1, 1)$ in the northeast-down system, respectively. The triangular source time function is applied to both LFEs and ordinary earthquakes, as we consider only the radiation pattern. Although the reflected waves at the Conrad and Moho discontinuities are considered in the ray tracing method of the real data, we do not include these effects for easier treatment in the forward calculations. As a result of the change in the ray path, the number of events analyzed in the synthetic test is less than that of the mechanism determination. The velocity model used for the synthetic waveforms was the JMA2001 velocity model (Ueno et al., 2002). We also calculated the quality factors for *P*- and *S*-waves, Q_P and Q_S, as follows:

$$Q_P = (v_p - 3.0) \times 200 \tag{1}$$
$$Q_S = 0.5 Q_P \tag{2}$$

where the *P*-wave velocity is v_p (km/s). We calculate density using the empirical relationship of Brocher (2005) as follows:

$$\rho = 1.6612 v_p - 0.4721 v_p^2 + 0.0671 v_p^3 - 0.0043 v_p^2 + 0.000106 v_p^5 \tag{3}$$

where the density is ρ (g/cm^3). We applied the same procedure described in Section 3.1. In this test, focal mechanisms are determined not only for pure synthetic waveforms but also for those with gaussian white noise with 0.1 nm/s a standard deviation.

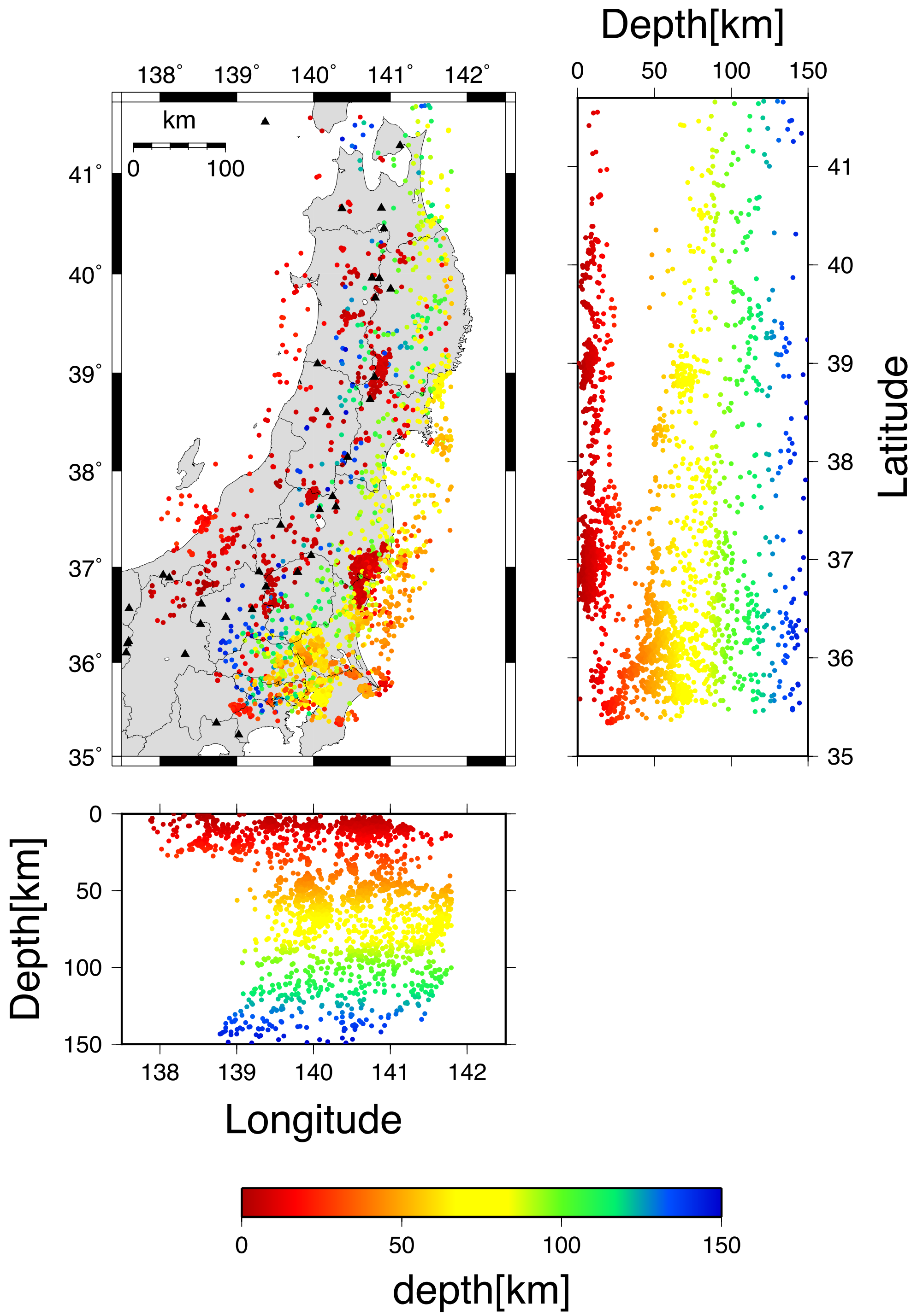

Figure S1. Map view and cross sections of ordinary earthquakes used for the station correction. The colors denote the focal depths, whose scale is shown at the lower-center. Black triangles represent active volcanoes.

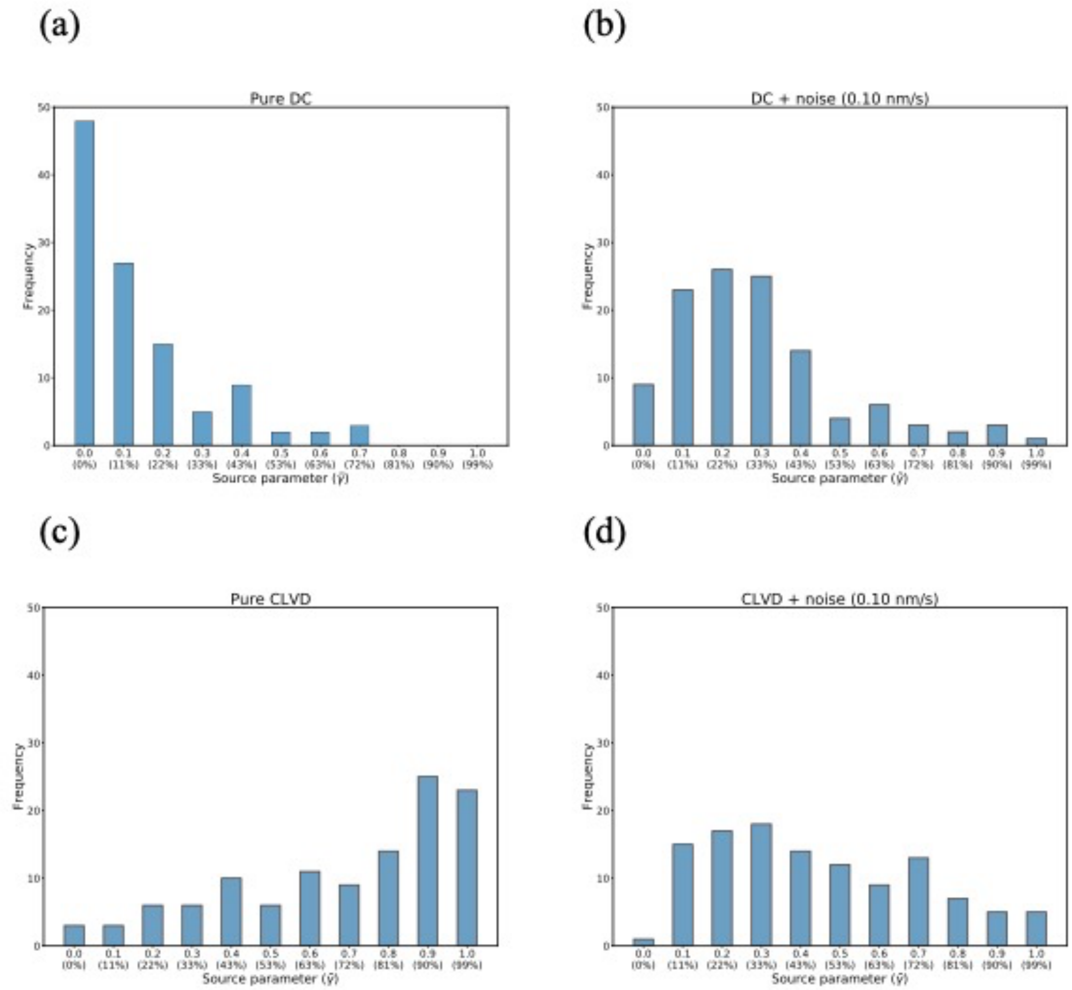

Figure S2. Same figure as Figure 6 but for synthetic test. (a) Pure double-couple source. (b) Pure double-couple source with gaussian white noise with 0.1 nm/s a standard deviation. (c) Pure CLVD source. (d) Pure CLVD source with gaussian white noise with 0.1 nm/s a standard deviation.

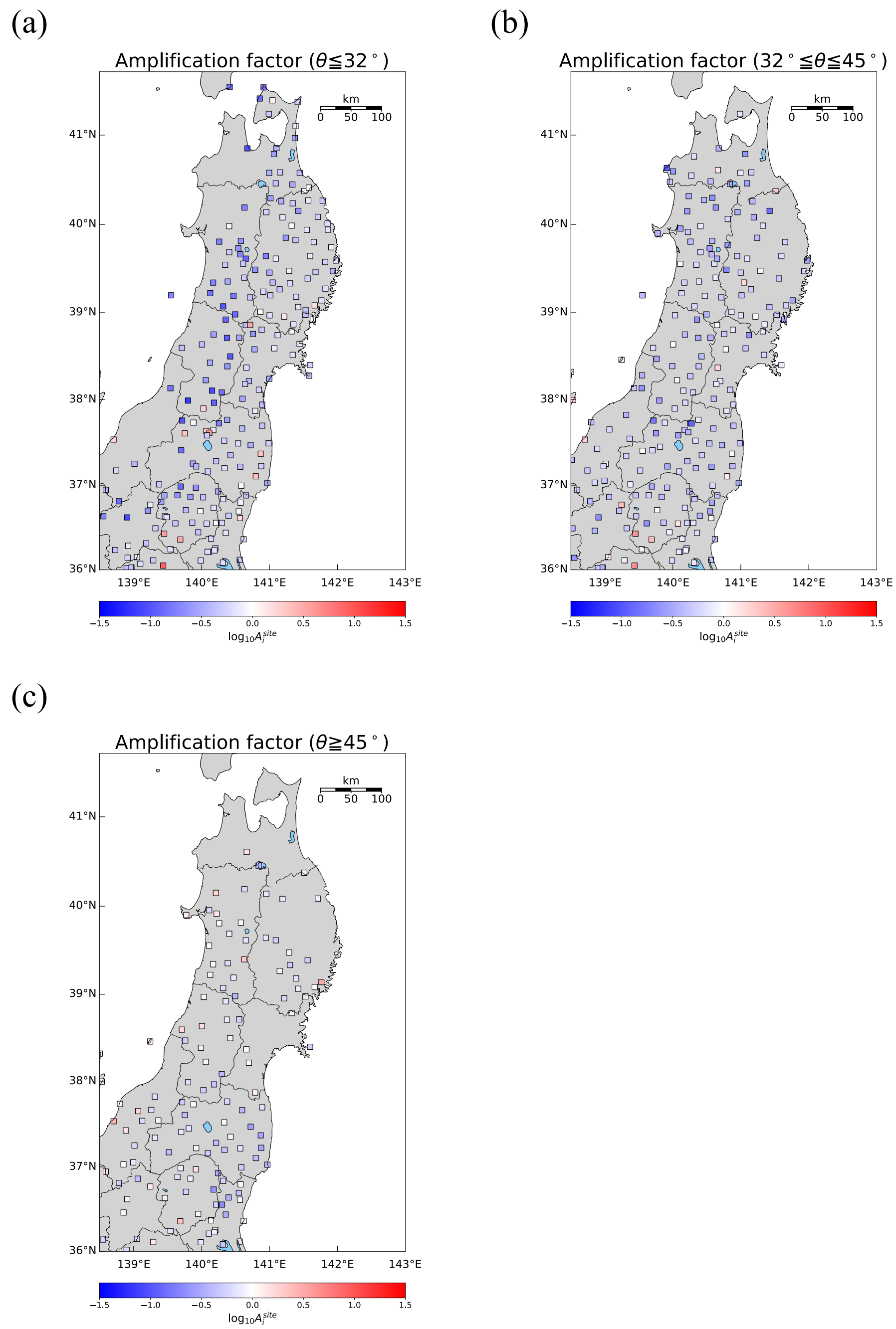

Figure S3. Map distribution of obtained station correction value. Plotted value is equal to $\log A_i^{site}$. The blue colored squares denote the stations with smaller observed amplitude ratios than theoretical, while the red colored squares denote the stations with larger observed amplitude ratios. (a) Station correction value for $\theta_{ij} \leq 32$. (b) Station correction value for $32 \leq \theta_{ij} \leq 45$. (c) Station correction value for $\theta_{ij} \geq 45$.

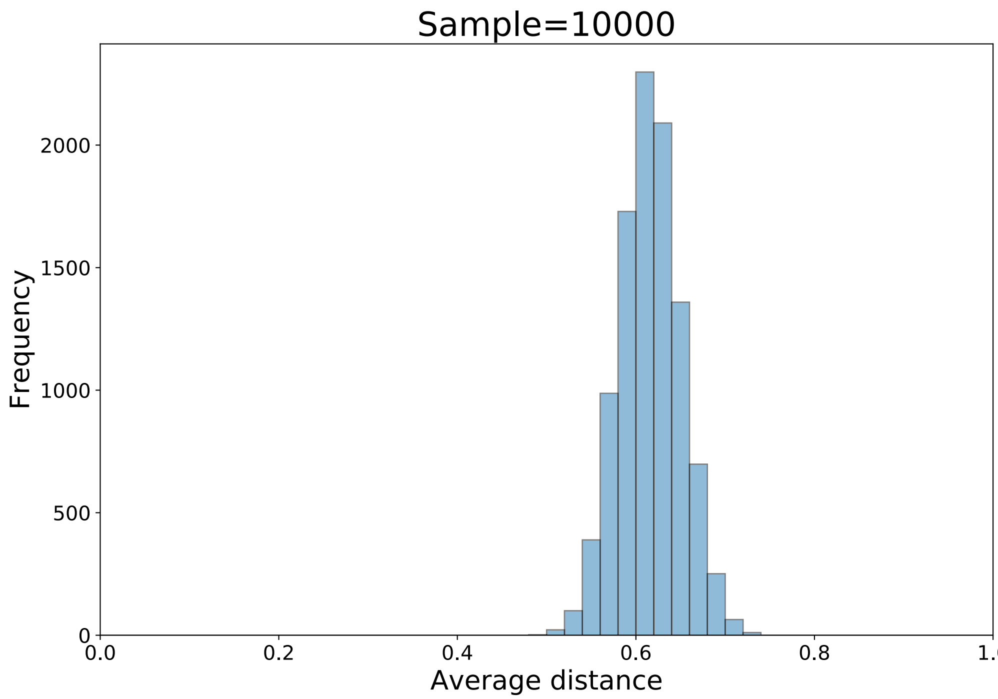

Figure S4. Frequency distribution of average distance in mechanisms. For each of 10000 randomly selected m_0, 100 different m_k are selected randomly and the average distance of d are calculated. The random mechanism is selected following independently and uniformly distributed strike, dip, and rake angles. Obtained distribution has peak around 0.6. Therefore, the threshold used in this study (0.4) is a suitable criterion for selecting stable solutions.

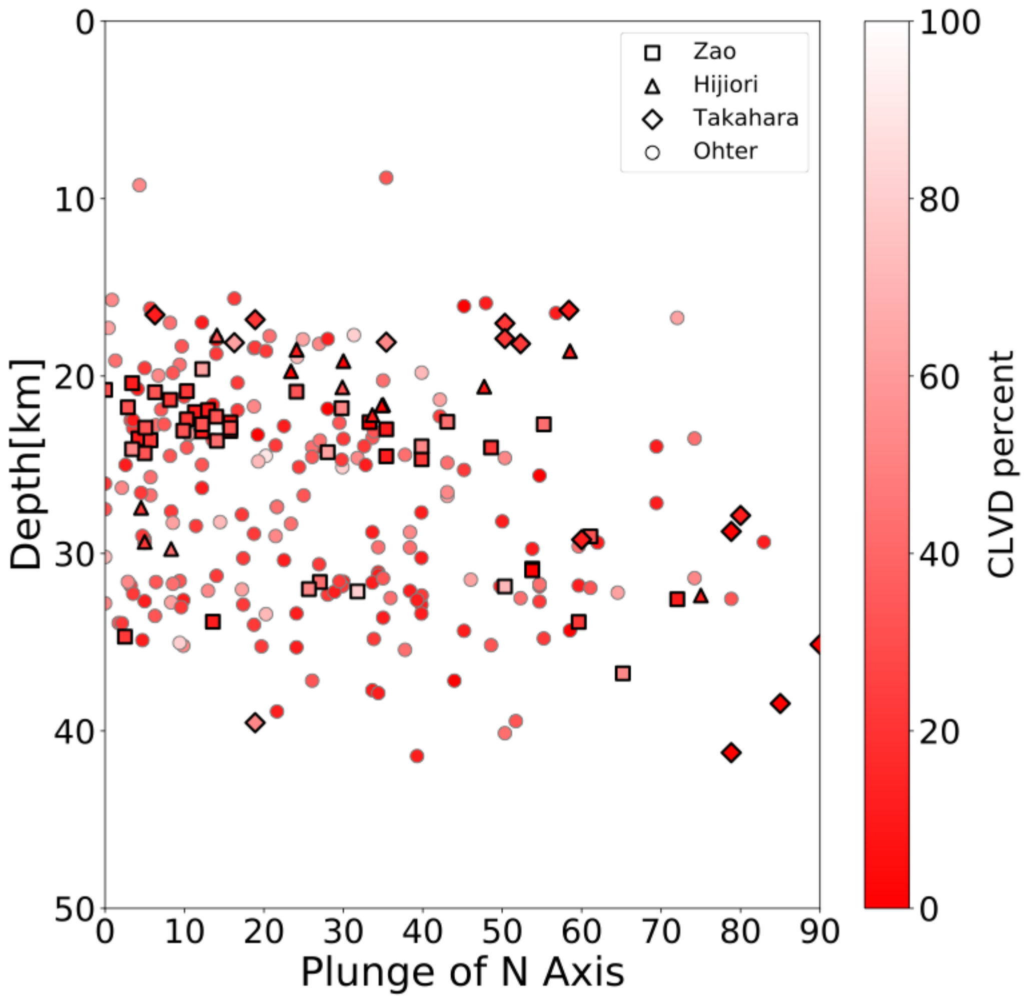

Figure S5. Null axis plunge angle for the selected LFEs in 26 regions as a function of depth. Plotted symbols are colored by the percentage of CLVD component. Square, triangle, and diamond symbols correspond to Zao, Hijiori, and Takahara, respectively.

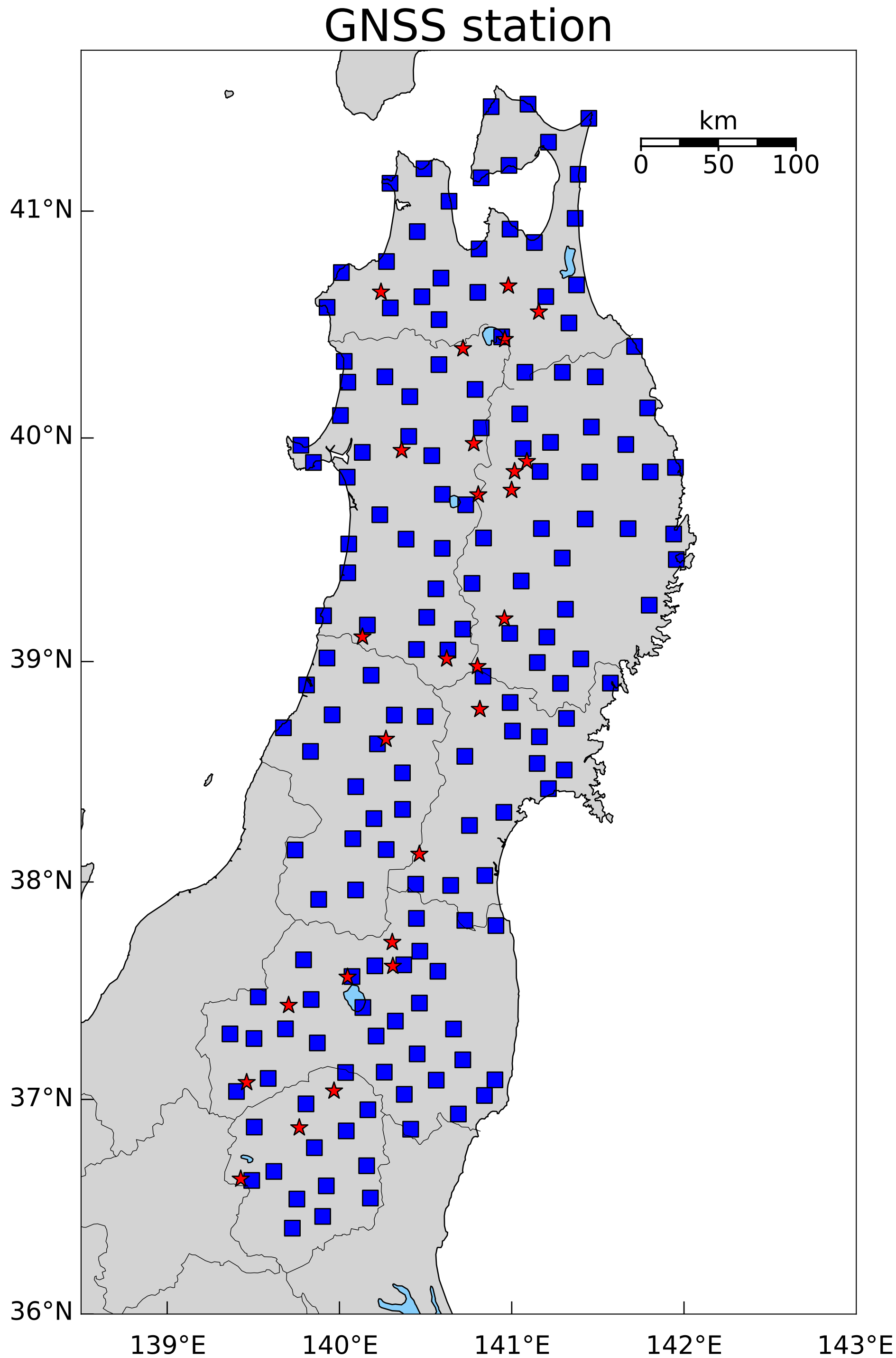

94

95 **Figure S6.** The map distribution of GNSS stations used for the estimation of time evolution
96 of afterslip. Blue squares denote the GNSS site and red stars indicates analyzed region in
97 this study, respectively. For this calculation, we use F3 solution published by the
98 Geospatial Information Authority of Japan.

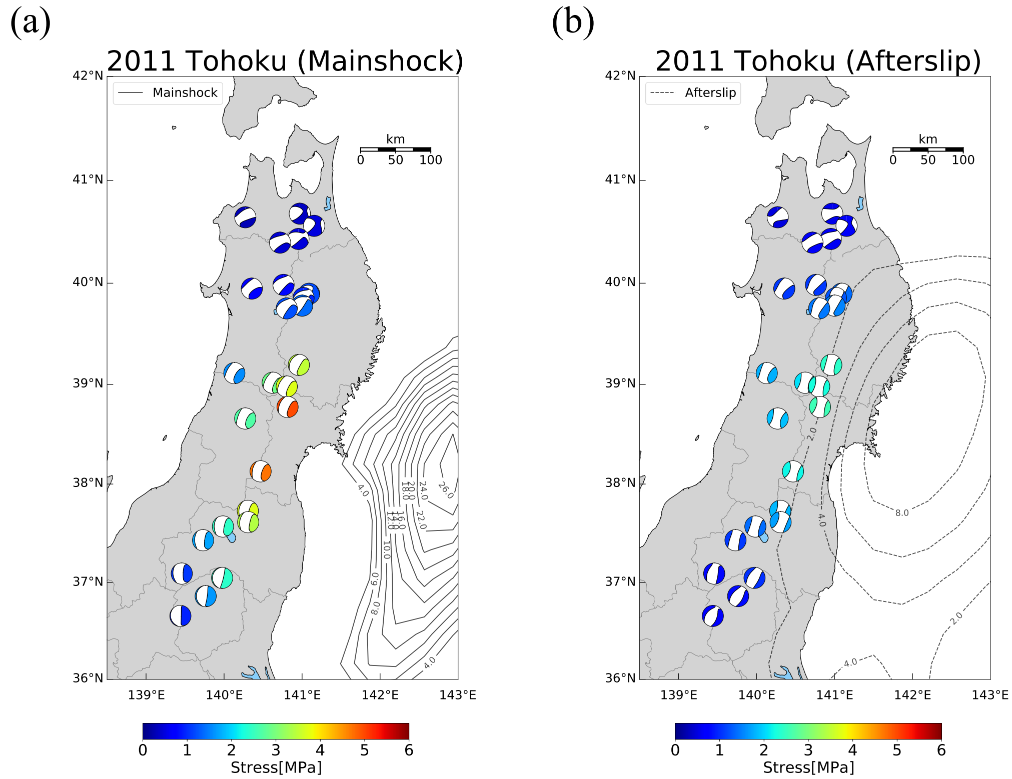

Figure S7. Induced stress tensors of mainshock (a) and afterslip (b) of the Tohoku earthquake. The color scale represents the absolute value of stress change.

References

Brocher, T. M. (2005). Empirical relations between elastic wavespeeds and density in the Earth's crust. Bulletin of the Seismological Society of America, 95(6), 2081–2092. https://doi.org/10.1785/0120050077

Ueno, H., Hatakeyama, S., Aketagawa, T., Funasaki, J., & Hamada, N. (2002). Improvement of hypocenter determination procedures in the Japan Meteorological Agency (in Japanese with English abstract. *Quarterly Journal of Seismology*, *65*, 123–134.

Zhu, L., & Rivera, L. (2002). A note on the dynamic and static displacements from a point source in multilayered media. Geophysical Journal International, 148(3), 619–627. https://doi.org/10.1046/j.1365-246X.2002.01610.x